

Dynamically disordered hydrogen bonds in the hureaulite-type phosphatic oxyhydroxide $\text{Mn}_5[(\text{PO}_4)_2(\text{PO}_3(\text{OH}))_2](\text{HOH})_4$

Cite as: J. Chem. Phys. 156, 094502 (2022); doi: 10.1063/5.0083856

Submitted: 30 December 2021 • Accepted: 8 February 2022 •

Published Online: 2 March 2022



A. Hartl,^{1,2} F. Jurányi,³ M. Krack,⁴ P. Lunkenheimer,⁵ A. Schulz,⁵ D. Sheptyakov,³ C. Paulmann,⁶ M. Appel,⁷ and S.-H. Park^{1,a)}

AFFILIATIONS

¹Department of Geo- and Environmental Sciences, Section of Crystallography, Ludwig Maximilian University (LMU) Munich, Theresienstraße 41 C, 80333 Munich, Germany

²Paul Scherrer Institute (PSI), Forschungsstrasse 111, 5232 Villigen, Switzerland

³Laboratory for Neutron Scattering and Imaging, PSI, CH-5232 Villigen PSI, Switzerland

⁴Laboratory for Materials Simulations, PSI, Forschungsstrasse 111, CH-5232 Villigen PSI, Switzerland

⁵Experimental Physics V, Center for Electronic Correlations and Magnetism, University of Augsburg, Universitätsstraße 1, 86159 Augsburg, Germany

⁶Institute of Mineralogy and Petrography, University of Hamburg, Grindelallee 48, 20146 Hamburg, Germany

⁷Institut Laue-Langevin (ILL), 71 Avenue des Martyrs, 38000 Grenoble, France

^{a)}Author to whom correspondence should be addressed: sohyun.park@lmu.de

ABSTRACT

We report the temperature evolution of hydrogen bond (HB) chains and rings in $\text{Mn}_5[(\text{PO}_4)_2(\text{PO}_3(\text{OH}))_2](\text{HOH})_4$ to reveal conduction pathways based on difference Fourier maps with neutron- and synchrotron x-ray diffraction data. Localized proton dynamics for the five distinct hydrogen sites were observed and identified in this study. Their temperature evaluation over ten orders of magnitude in time was followed by means of quasielastic neutron scattering, dielectric spectroscopy, and *ab initio* molecular dynamics. Two out of the five hydrogen sites are geometrically isolated and are not suitable for long-range proton conduction. Nevertheless, the detected dc conductivity points to long-range charge transport at elevated temperatures, which occurs most likely (1) over H4–H4 sites between semihelical HB chains (interchain-exchanges) and (2) by rotations of O1–H1 and site-exchanging H4–O10–O5 groups along each semihelical HB chain (intrachain-exchanges). The latter dynamics freeze into a proton-glass state at low temperatures. Rotational and site-exchanging motions of HOH and OH ligands seem to be facilitated by collective motions of framework polyhedra, which we detected by inelastic neutron scattering.

Published under an exclusive license by AIP Publishing. <https://doi.org/10.1063/5.0083856>

I. INTRODUCTION

For exploring efficient and sustainable compounds for energy storage and conversion in batteries and fuel cells, there is an ecologically and economically friendly approach to use the lightest element hydrogen as the mobile species in electrochemical systems.¹ Several proton conductors exhibiting high ionic conductivity under ambient conditions have been proposed in recent studies.^{2,3} In particular, solid acids have been considered as promising proton conductors^{4–7} because they can enter a superprotonic state with an

ionic conductivity value of $10^{-2} \text{ S cm}^{-1}$ at room temperature.⁸ Among them, by considering high thermal stability and chemical flexibility,^{4,9} phosphatic oxyhydroxide minerals can serve as prototype matrices for conducting protons according to the concept of dynamically disordered hydrogen bonds (DDHBs), where charge transport proceeds via conducting protons of hydrogen bonds (HBs), e.g., CsH_2PO_4 ^{10,11} and KH_2PO_4 .^{12,13} It is, however, rare to find related research that goes beyond time-averaged data in order to explain the underlying proton conduction mechanisms concretely. Furthermore, the concerted behavior of protons

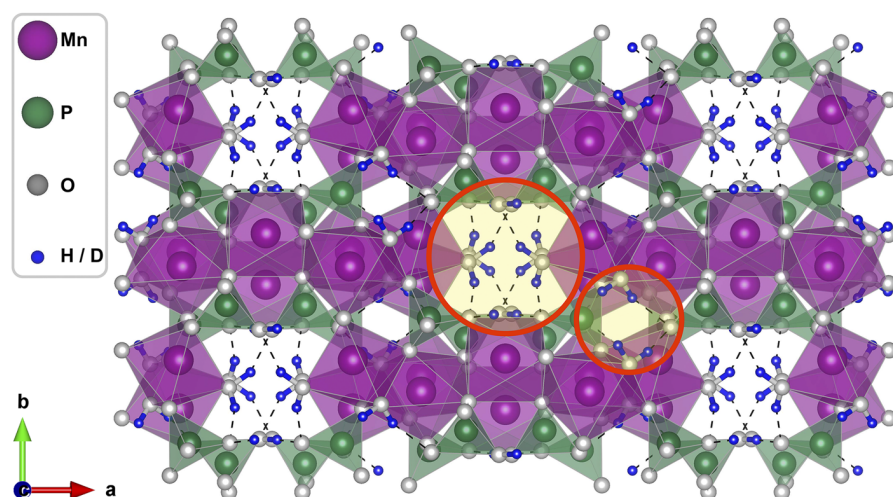


FIG. 1. Structure of deuterated Mn-hureaulite at 12 K¹⁴ with emphasis on the HB system. The octahedral–tetrahedral framework, built out of Mn(DO, DOD)₆ (pink) and P(O, OD)₄ (green), features one-dimensional 8MR-channels running along the *c* axis. Each channel contains an enantiomorphic pair of semihelical HB chains (large red circle). In addition, there are small HB rings in cage-like pores (small red circle). Mn, P, O, and D atoms are illustrated in pink, green, pale gray, and blue, respectively, along with HBs highlighted by broken lines in black.

and its “host lattice” needs to be explained under several conditions in order to understand and apply the complex mechanisms for charge transport via protons. The current study is dedicated to quantitatively elucidate time and length scales of various proton motions over HB-chains and HB-rings in a manganese phosphatic oxyhydroxide, Mn₅[(PO₄)₂(PO₃OH)₂](HOH)₄ (space group: C2/c; *Z* = 4) (denoted as Mn-hureaulite hereafter), based on the successful synthesis and characterization of pure Mn-hureaulite samples.¹⁴

Our recent neutron powder diffraction study of deuterated Mn-hureaulite (Mn₅[(PO₄)₂(PO₃OD)₂](DOD)₄) showed that pentamers of edge-sharing [Mn(O, DOD)₆] octahedra comprise complex cross spin-canting configurations.¹⁵ Those Mn-pentamers are connected to each other via P(O, OD)₄ tetrahedra. As a result, this octahedral–tetrahedral framework features a one-dimensional 8-membered ring (8MR) channel system running along the crystallographic *c* axis and cage-like pores with a small 4MR-opening, as highlighted in Fig. 1. In the hureaulite-type compounds, protons are structurally bonded to the framework polyhedra as HOH or OH ligand groups. When describing HBs in its deuterated form, there are two facing D2–O9–D3 groups to make a small HB ring in the confined cage, while D1–O1 and D4–O10–D5 groups form one pair of semihelical HB chains in each 8MR-channel. Their configurations give rise to several possible pathways for site-exchanging protons, as shown in Fig. 2: rotations and site-exchanges at O1–D1, D4–O10–O5, and D2–O9–D3 [Figs. 2(a) and 2(d)]; intrachain-exchanges between O1–D1 and D4–O10–O5 groups [Fig. 2(a)]; and interchain-exchanges via D4–D4, D5–D5, and D4–D5 between two semihelical chains [Figs. 2(a)–2(c)]. The dynamic disorder of protons over such sites and routes represents an interesting object for both experimental and theoretical studies of complex proton behaviors.^{3,16–23} Furthermore, according to Baranov,⁸ hureaulite shows a high theoretical intrinsic charge carrier concentration of $N_p = 2.629 \times 10^{22}$ protons per cm³, exceeding the boundary value $N_{p, \text{limit}} = 10^{18}$ protons cm^{−3} between high and low proton mobility.²⁴ This motivated us to resolve a consistent picture of charge transport via protons over the DDHBs in this complex system by diffraction and spectroscopy tools in combination with

density functional theory (DFT) based *ab initio* molecular dynamics (AIMD) simulations performed with the CP2K code, as described below.

II. METHODS

A. X-ray single crystal diffraction (XSD)

X-ray single crystal diffraction (XSD) was applied to monitor the response of the framework of Mn-hureaulite to temperature changes. For this purpose, single crystals of the title compound were obtained via hydrothermal synthesis, as described in the previous study.¹⁴ Each crystal sample with a size of $10 \times 20 \times 100 \mu\text{m}^3$ was selected and attached to silica glass wires using a double-component adhesive and alumina paste for low-temperature (LT) and high-temperature (HT) XSD, respectively.

A series of LT-XSD was performed between 100 and 295 K on a four-circle κ single crystal diffractometer (Gemini A Ultra) equipped with a 2D charge-coupled detector (135 mm active area diameter, Atlas) from Rigaku-Oxford Diffraction. LT-XSD data collection was carried out with (MoK α_1) radiation [graphite (002) monochromator] in a crystal-to-detector distance of 60 mm with a step size of $\Delta(\phi) = 1^\circ$. The temperatures were controlled using an open nitrogen cryostat (Cryojet 02, Oxford Instruments) ($\Delta T < \pm 0.1$ K). Data collection and reduction were performed using the software package CrysAlisPro.²⁵ Absorption corrections were done using the SCALE3 ASPACK scaling algorithm implemented in CrysAlisPro.

HT-XSD was conducted at the experimental station P24 at the synchrotron radiation source PETRA III at Deutsches Elektronen-Synchrotron (DESY). HT-XSD datasets were collected between 300 and 500 K every 50 K in sequence at elevated temperatures on a four-circle κ single crystal diffractometer using a wavelength of $\lambda = 0.49594 \text{ \AA}$ [Si(111) monochromator]. The temperatures were set via a nitrogen gas stream heater. All HT-XSD data were acquired on a 2D Pilatus detector (CdTe 1M) with a crystal-detector distance of 60 mm in ω/ϕ scans having a scan width of 1.0° . Raw HT-XSD data were converted to the CCD format of Atlas for integration and reduction processes using CrysAlisPro. Further experimental parameters and details on refinements of LT- and HT-XSD

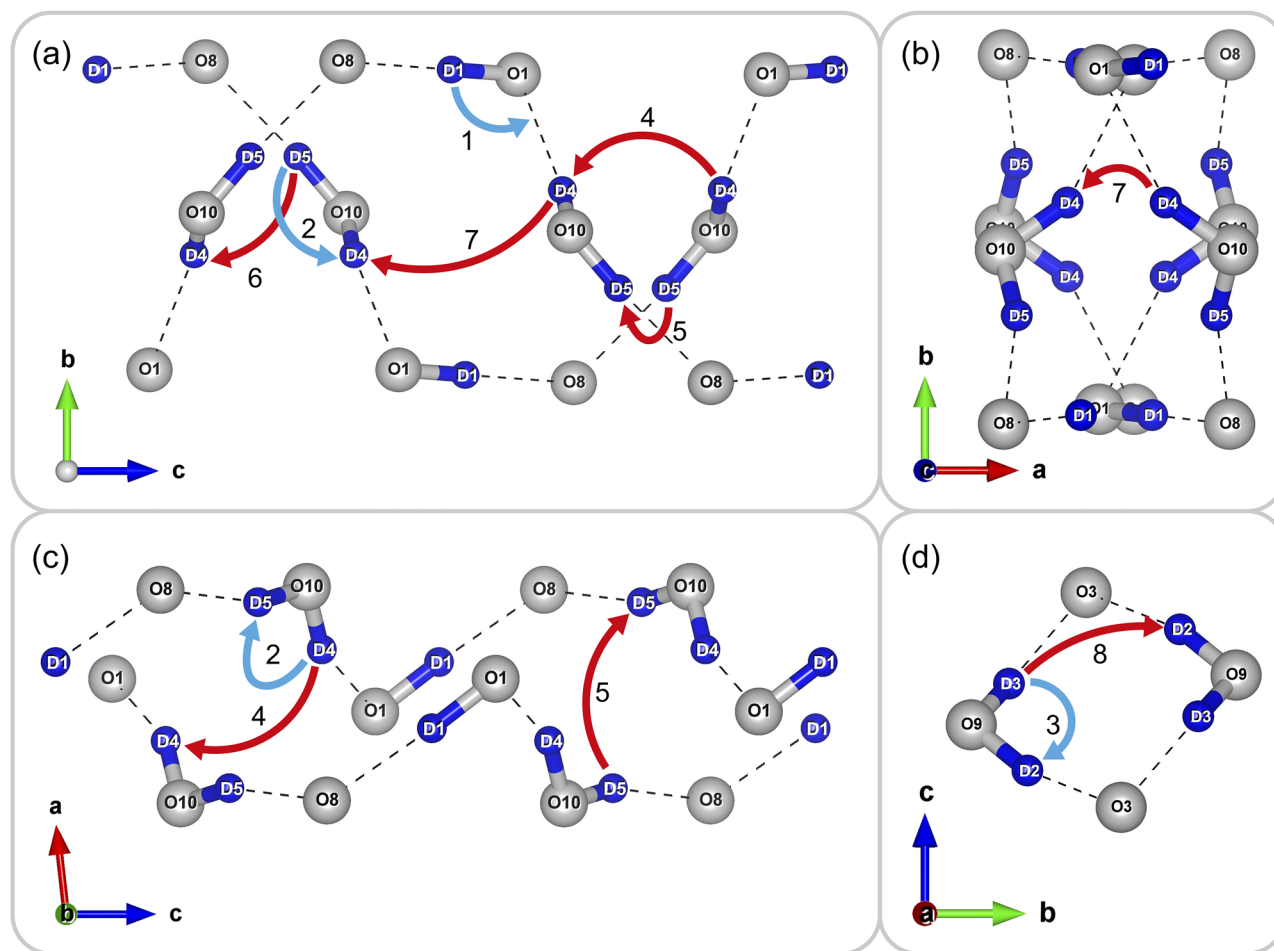


FIG. 2. Representative sections of HBs in Mn-hureaulite (deuterated): (a) a pair of two HB chains projected on the (b) and (c) plane; (b) through the 8MR-channel opening; (c) projected on the (a)-(c) plane; and (d) a HB-ring of two D2-O9-D3 groups located within small 4MR cages. There are several possible routes for locally limited, rotational site-exchange (in blue), as well as inter- and intrachain exchanging motions (in red): (1) rotating O1-D1 group along the HB chain; (2) local rotation of D4 and D5 in a D4-O10-D5 group; (3) rotation of D2 and D3 in a D2-O9-D3 group; (4) interchain exchange of D4 and D4 between semihelical HB chains; (5) interchain exchange of D5 and D5 between two semihelical HB chains; (6) interchain motion cross over D4 and D5; (7) long-range proton dynamics over D4-D4 pairs; and (8) hopping motions between two D2-O9-D3 groups.

conducted in this study are given with agreement factors in Secs. A and B of the [supplementary material](#).

Structure refinements with XSD data were carried out by the least-squares method against the squared structure factor (F^2) with an option of difference Fourier (ΔF) synthesis, implemented in the Jana2006 program.²⁶ An initial starting model delivered by Rietveld analyses using high-resolution neutron powder diffraction (HRNPD) data at room temperature in our previous study¹⁴ was used for structure refinements with LT- and HT-XSD datasets collected at room temperature. The refined models were used as the successive starting models for further analyses with LT- and HT-XSD data. For each structure refinements, all atomic sites were fixed to be fully occupied because of high correlations between occupancy and atomic displacement parameters (ADPs), in addition to the low x-ray scattering power of light elements. All atomic

parameters, including anisotropic atomic displacement parameters (ADPs) at Mn, P, and O sites, as well as isotropic ADPs at five independent H sites, could be refined simultaneously without high correlations (<0.9). The refined atomic parameters are given in Sec. C of the [supplementary material](#) along with the obtained interatomic distances and angles in HBs.

B. High-resolution neutron powder diffraction (HRNPD)

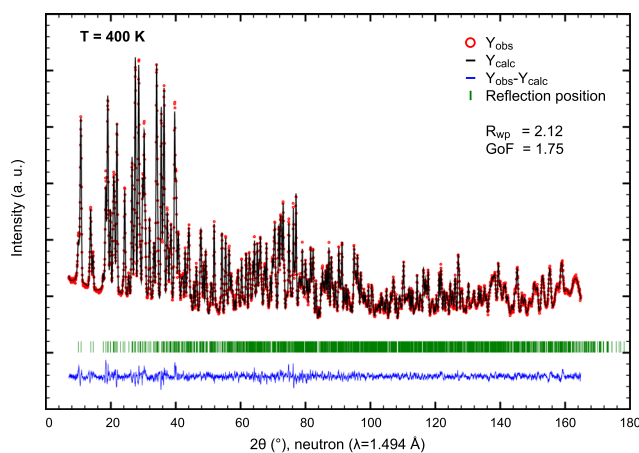
We used HRNPD to determine the positions and ADPs of light elements accurately. These experiments have been performed on deuterated Mn-hureaulite because of the pronounced coherent neutron scattering cross section of deuterium (D) in contrast to the huge incoherent neutron scattering cross section of hydrogen (H).

TABLE I. Experimental and refinement parameters of HRNPD probed on deuterated Mn-hureaulite. The applied R factors are mathematically expressed in Sec. B of the [supplementary material](#).

Refinement parameters	150 K	250 K	350 K	400 K
a (Å)	17.582 70(19)	17.605 82(16)	17.641 7(2)	17.656 9(2)
b (Å)	9.121 38(12)	9.129 56(9)	9.149 43(13)	9.159 58(14)
c (Å)	9.492 71(11)	9.495 08(9)	9.502 68(11)	9.505 95(11)
β (°)	96.421 5(7)	96.449 1(4)	96.480 7(8)	96.491 2(9)
V (Å ³)	1512.88(3)	1516.52(3)	1524.04(3)	1527.54(3)
Number of model atoms	20	20	20	20
Number of refined parameters	150	156	156	229
R factors (%)				
R [reflections with $I > 3\sigma(I)$]	1.59	1.42	1.47	1.26
wR2 [reflections with $I > 3\sigma(I)$]	2.00	1.72	1.86	1.58
Profile R factors (%)				
GoF	1.69	1.57	1.66	1.72
Rp	2.34	2.05	1.91	1.64
wRp	2.97	2.57	2.41	2.07

Variable-temperature HRNPD datasets allowed us to differentiate between dynamic and static disorders. Furthermore, the pathways possible for the protonic conductivity can be estimated by inspecting the residual densities of coherent neutron scattering length distribution of D in ΔF maps.

For HRNPD, 1.8 g of deuterated Mn-hureaulite powder was air-tightly closed in a vanadium can ($\emptyset = 12$ mm). HRNPD datasets were collected on the instrument HRPT at SINQ, PSI, Switzerland, using $\lambda = 1.494$ Å with the medium resolution setup at 150, 250, 350, and 400 K, subsequently.

**FIG. 3.** Representative Rietveld refinement of HRNPD data of deuterated Mn-hureaulite at 400 K with agreement factors. The calculated profile (black line) is well matched to the observed one (red circles), as shown by their low difference profile (blue line). Short bars indicate Bragg reflection positions expected for the atomic structure of Mn-hureaulite in the space group C2/c.

Rietveld calculations were executed using the program package Jana2006. The background was fitted with a Legendre polynomial of 36 terms. Profile parameters were described by Pseudo-Voigt function, including a preferred orientation of the 110 reflection via the March–Dollase approach.

Large ADPs can result from the depletion of atoms away from their equilibrium sites not only due to dynamic disorder but also due to partial occupation. Hence, to prevent high correlations between occupancy and APD parameters, all atomic parameters were refined with full occupations at all atomic sites. Under this condition, all five unique D sites could be refined simultaneously with their anisotropic ADPs at all measuring temperatures. ADPs of O, P, and Mn atoms at 150 and 250 K were refined direction-independently only, while those of O and P at 350 K could be refined anisotropically. At 400 K, ADPs of the entire atoms, including Mn sites, could be determined anisotropically without high correlations with good agreement factors (Table I; Fig. 3). All atomic parameters refined with HRNPD datasets are found in Sec. D.1 of the [supplementary material](#). The resulting interatomic distances and angles of HBs are given in Table II.

C. Neutron spectroscopy

Quasielastic neutron scattering (QENS) was performed to measure the characteristic time and length scales of both local and diffusional motions. Inelastic neutron scattering (INS) was used to obtain the lattice dynamics. QENS and INS data acquisitions were carried out on the time-of-flight spectrometer, FOCUS at SINQ (PSI) with a sample of 0.802(1) g powdered Mn-hureaulite, enclosed in a hollow cylindrical Al sample can. The sample was protonated in order to emphasize the mobile hydrogen atoms of OH and HOH groups via the large incoherent neutron scattering length. For measurements up to 510 K, $\lambda = 6$ Å was used with an energy resolution of 45 μ eV.

TABLE II. Interatomic distances and angles of hydrogen bonds analyzed by HRNPD of deuterated Mn-hureaulite from 150 to 400 K.

HRNPD	Donor O _D	D site	Acceptor O _A	d(D-O _D) (Å)	d(D ··· O _A) (Å)	d(O _D -O _A) (Å)	∠(O _D -D ··· O _A) (°)
150 K	O1	D1	O8	1.001(4)	1.581(4)	2.581(4)	176.7(4)
	O9	D2	O3	0.963(5)	1.871(5)	2.771(5)	154.4(4)
	O9	D3	O3	0.989(5)	1.684(5)	2.653(5)	165.5(4)
	O10	D4	O1	0.965(5)	1.838(5)	2.723(5)	151.2(4)
	O10	D5	O8	0.985(5)	1.749(5)	2.707(5)	163.1(4)
250 K	O1	D1	O8	1.007(4)	1.602(4)	2.608(4)	175.9(4)
	O9	D2	O3	0.956(5)	1.893(5)	2.781(5)	153.4(3)
	O9	D3	O3	0.980(5)	1.694(5)	2.656(5)	166.1(4)
	O10	D4	O1	0.970(6)	1.848(5)	2.739(5)	151.3(4)
	O10	D5	O8	0.981(6)	1.761(5)	2.714(5)	163.0(4)
350 K	O1	D1	O8	1.006(5)	1.618(4)	2.621(4)	174.4(4)
	O9	D2	O3	0.970(5)	1.907(5)	2.806(5)	153.0(4)
	O9	D3	O3	0.976(5)	1.707(5)	2.664(5)	165.9(4)
	O10	D4	O1	0.965(6)	1.871(6)	2.754(6)	151.0(5)
	O10	D5	O8	0.988(6)	1.762(6)	2.721(6)	162.7(4)
400 K	O1	D1	O8	0.987(5)	1.632(5)	2.615(5)	173.1(5)
	O9	D2	O3	0.965(6)	1.923(6)	2.814(6)	152.4(4)
	O9	D3	O3	0.958(6)	1.722(6)	2.662(6)	166.5(4)
	O10	D4	O1	0.973(7)	1.863(8)	2.750(7)	150.1(6)
	O10	D5	O8	0.976(8)	1.790(7)	2.740(6)	163.6(5)

Data treatment and analysis was done with the DAVE software.²⁷ In the paramagnetic state of Mn-hureaulite above 6.17 K,¹⁵ the magnetic QENS signal showed no significant temperature-dependence. Additional QENS signal with comparable intensity appeared above 250 K. Therefore, the 250 K measurement was used as background. The observed QENS signals are given in the [supplementary material](#) (Fig. E.1), where the paramagnetic contribution (and the background) is subtracted using the 250 K data.

A fixed window scan (FWS) between 2 and 483 K was performed on the high-resolution backscattering spectrometer IN16B at ILL, France, using $\lambda = 6.271$ Å with an energy resolution of 0.75 μeV. Simultaneously, inelastic fixed window scan (IFWS) was recorded with the offset energy of 3 μeV, where the contribution from elastic scattering was small enough. FWS and IFWS data were alternately collected during heating with a rate of 1 K/min (see Sec. F of the [supplementary material](#)). The data treatment was performed according to the instrument standard software Mantid.

D. Dielectric spectroscopy (DS)

Dielectric spectroscopy (DS) allows us to probe time scales for changing orientations and dislocations of charge carriers. The measured real part of the capacitance and the conductance allows us to evaluate the dielectric properties, such as the respective real part of the dielectric constant ϵ' and conductivity σ' .

For DS studies, powder samples of both protonated and deuterated Mn-hureaulite were pressed into compact pellets, and then their top and bottom sides were coated with conductive silver paste. “Low frequency” (LF) dielectric spectra were acquired between

1 Hz and up to several MHz using a frequency response analyzer (Novocontrol Alpha analyzer). Additional data acquisitions in the “high frequency” (HF) range between 1 MHz and 3 GHz were performed employing an impedance analyzer (Keysight E4991B). For this reflectometric technique,²⁸ the sample was placed at the end of a coaxial line so that it bridged the inner and outer conductor. The temperature in the sample cell was controlled using a continuous flow N₂-gas cryostat (Novocontrol Quatro).

For the correction of $\epsilon'(T)$, an additive factor was applied in the low-temperature (LT) region ($T < 200$ K) of the HF data collected with the coaxial technique. The LF spectra were scaled with respect to the HF data due to stray capacitance effects and parasitic capacitance from the geometry of the setup in the frequency response analysis.

E. *Ab initio* molecular dynamics (AIMD) simulations

The complex, distorted framework polyhedral units and the particular proton sites in Mn-hureaulite made it insufficient to apply molecular dynamics (MD) calculations based on predefined interatomic potentials (force fields). In addition, the impact of the antiferromagnetic sublattice formed by the Mn atoms cannot be captured by a force field approach. Thus, AIMD calculations were executed for this system, where the forces acting on the atoms were calculated based on first principles.²⁹ We took advantage of the efficient implementation of Born–Oppenheimer AIMD within the program package CP2K.³⁰ Its DFT module QUICKSTEP³¹ employs a mixed Gaussian and plane wave basis set. The scalar-relativistic, norm-conserving pseudopotentials of Goedecker–Teter–Hutter (GTH)^{32–34} for Mn ($3s^2 3p^6 3d^5 4s^2$),

P ($3s^2 3p^6$), and O ($2s^2 2p^6$) were used to avoid an explicit consideration of the core electrons. Unless otherwise stated, we employed the short-range double-zeta Gaussian (MOLOPT) basis sets with one set of polarization functions (DZVP-SR)³⁵ that were optimized for the GTH pseudopotentials. All calculations were performed with the spin-polarized implementation of the Perdew, Burke, and Ernzerhof (PBE) exchange-correlation functional.³⁶ The empirical dispersion correction DFT-D3 of Grimme *et al.*³⁷ for PBE was applied for an improved description of the van der Waals interactions. An electronic density cutoff of 600 Ry and the orbital transformation (OT) method for self-consistent field (SCF) calculations with a convergence threshold of 3×10^{-7} for the wave function gradient were used in all calculations.

In sum, these computational parameters usually showed good agreement with experiment. Indeed, the optimized structure corresponded well to those refined with HRNPD data ($\pm 0.3\%$). Structural relaxations and bandgap calculations at 0 K for a single ($1 \times 1 \times 1$) Mn-hureaulite unit cell (156 atoms) with a Γ -centered $4 \times 8 \times 8$ k -point mesh using the VASP code version 5.4.4^{38,39} agreed well with the corresponding CP2K results for a $1 \times 2 \times 2$ supercell (624 atoms). Further technical details about the Mn-hureaulite simulations can be found in Sec. G of the [supplementary material](#).

A $1 \times 2 \times 2$ supercell of the Mn-hureaulite system was initially equilibrated for at least 10 ps within the isobaric-isothermal NpT ensemble at the pressure 1 bar and at three temperatures, 300, 350, and 400 K. The average cell parameters of the last 8 ps from the NpT MD trajectories were then used for the thermalization runs within the canonical ensemble (NVT). Finally, MD runs within the microcanonical ensemble (NVE) were performed, which are free of any bias or frequency coupling from a barostat or thermostat. The energy drift along the NVE trajectories was fairly small ($\ll 1$ K/atom), indicating a very good quality of these MD runs. The corresponding average temperatures of these NVE MD runs were 301, 379, and 511 K. The MD runs at 300 K were sampled with a time step of 0.5 fs, whereas the MD runs at the higher temperatures required a shorter time step of 0.4 fs. The program TRAVIS^{40,41} was used for the post-processing of the MD trajectories. The vector-meson dominance (VMD) Molecular Graphics Viewer helped for visualization purposes.⁴²

The density of states (DOS) for each characteristic proton site could be derived by the Fourier transform of the time dependent velocity-velocity autocorrelation function of the corresponding AIMD trajectories.^{43,44} In comparison to simulated Raman modes, this approach took anharmonic effects into account and helped to explain proton-site-dependent contributions to generalized density of states (GVDOS) delivered from INS techniques.

III. RESULTS AND DISCUSSION

A. Structural response to temperature, observed in diffraction studies

1. Thermal responses of the framework

The temperature dependence of the unit cell parameters reveals strongly anisotropic thermal expansion, which is along the crystallographic c axis distinctively smaller than in the a and b directions [see the [supplementary material](#), Figs. D.2(a)–D.2(c)]. This

means that the one-dimensional channels running parallel to the c axis are widened in the (a) and (b) plane, i.e., perpendicular to the semihelical HB chains [see Fig. D.2(e) in Sec. D.3 of the [supplementary material](#)]. As a result, at elevated temperatures, the framework of Mn-hureaulite favors its OH and HOH ligand groups readily mobile toward the channel system. This promotes a distortion of the HB geometry, which can directly impact the long-range and local proton dynamics, e.g., the site-exchanging processes over O1–H1 and H4–O10–OH5 ligands within the 8MR-channel.

The eigenvalues U_i of anisotropic ADPs refined with XSD data (see Sec. C.1 of the [supplementary material](#)) show large values at the oxygen sites, particularly for those of H4–O10–H5, O1–H1, and H2–O9–H3 groups. More interestingly, at elevated temperatures, U_3 values of all framework atoms distinctly enlarge in contrast to U_1 and U_2 values (Fig. D.1 of the [supplementary material](#)). For instances, the “double” acceptor site O10 of the H4–O10–H5 group within the semihelical HB chain shows U_3 being 2.8 times larger than U_1 at 500 K. In contrast, another “double” acceptor site O9 of the H2–O9–H3 HB within the small cage shows much smaller ADP eigenvalues in comparison to O10. These observations indicate dynamic disorder profoundly occurring over the semihelical HB chains.

The thermal response of the entire Mn-hureaulite framework can be discussed with ΔF maps evaluated with XSD data: Once ΔF maps are generated with all atomic sites refined but without H atoms, positive electron density peaks are accumulated at the expected H atom sites below 250 K but smeared out around the semihelical HB-chains at 300 K (Fig. C.1 of the [supplementary material](#)). They become more diffuse at elevated temperatures, reflecting the DDHB chains for proton dynamic disorder. At the same time, diffuse and positive ΔF densities are observed around the framework polyhedra, as well. This can be explained by superimposed anharmonic ADP terms of Mn, P, and O atoms, which may be a sign for their collective motions remarkably enhanced at $T \geq 300$ K (Fig. C.1). This reminds us of a redistribution of electron density residuals for fast rotating polyhedra in the superionic conductor γ -Na₃PS₄,⁴⁵ where strong electron density residuals were attributed to several possible oxygen positions around the tetrahedrally coordinated phosphorous cations. At $T \geq 300$ K, the electron density residual around the HB-ring within small cages in Mn-hureaulite increasingly redistributes, i.e., from O9 of H2–O9–H3 [related to Type 3 in Fig. 2(d)] toward the opposite oxygen site O3 [related to Type 8 in Fig. 2(d)].

In the following, we trace motions of deuterium atoms (D) occupying five independent sites in the deuterated Mn-hureaulite structure by means of their temperature-dependent ADP eigenvalues accurately determined by Rietveld analyses of the HRNPD data. When comparing these values between 150 and 400 K (Fig. 4), several site- and direction-dependent changes of ADPs are obvious, such as:

- (1) $U_3 \gg U_2 > U_1$ is valid for all D sites. The commonly strong increase of their U_3 at elevated temperatures points a strong dynamic disorder of HBs along the c direction.
- (2) At 250 K, $U_3(D_4)$ and $U_3(D_5)$ are larger than U_3 at the rest D sites, pointing re-orientations within a D4–O10–D5 group (see Type 2 in Fig. 2(a)).

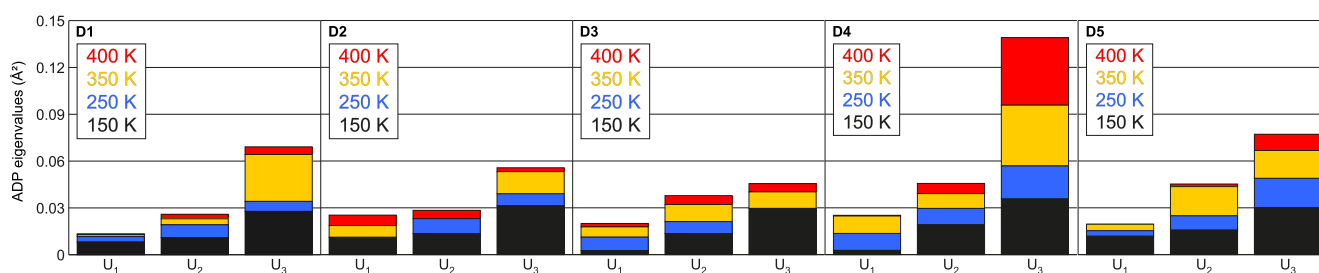


FIG. 4. Comparisons of temperature-dependent eigenvalues of anisotropic APDs at five independent deuterium sites, obtained from HRNPD data of deuterated Mn-hureaulite.

- (3) At 350 K, $U_3(D_4)$ is dramatically enlarged, accompanied by an increasing $U_3(D_5)$, as well as $U_2(D_5)$ and $U_3(D_1)$. This is an important sign for the onset of intrachain-exchanges over D1 and D4 and maybe also for the onset of interchain-exchanges over D4 and D5 [Types 1, 4, and 5, respectively, in Fig. 2(a)].
- (4) In addition, $U_3(D_2)$ increases obviously from 350 to 400 K along with $U_3(D_3)$, indicating re-orientations within a D2-O9-D3 group confined in a 4MR-cage and/or the onset of inter-ring-exchanges of a pair of D2-O9-D3 groups. Their motions are connected with Type 3 and Type 8 in Fig. 2(d), respectively.
- (5) $U_3(D_4)$ solely keeps profoundly increasing up to 400 K. This corresponds to the site-exchange in Type 4 but also is a hint for high dynamic disorder over D4 sites in an extended path, e.g., Type 7 in Figs. 2(a) and 2(b).

2. DDHBs in Mn-hureaulite

XSD probes the electron density of the polarized hydrogen bond and not the nuclear position. Thus, the resulting interatomic distances in HBs are underestimated (see Sec. C.2 of the [supplementary material](#)). For this reason, the role of DDHBs for charge transport properties in the title compound is discussed based on the results from HRNPD data analyses. These showed that, from 150 to 400 K, the distance $d(D-O_A)$ between deuterium (D) and the oxygen acceptor (O_A) increases (Table II). At the same time, the HB angles $\angle(O_D - D \cdots O_A)$ slightly decrease with the temperature at $D_5 < D_4 < D_3 < D_2 < D_1$. Overall, according to T -dependent HB-lengths and HB-angles, the HBs in Mn-hureaulite correspond to moderate HB strengths and remain stable up to the first dehydration at 538 K.¹⁴

ΔF maps evaluated with HRNPD data revealed diffuse elastic neutron scattering length densities at 350 and 400 K (Fig. 5; Figs. D.3 and D.4 of the [supplementary material](#)). Their maximal intensities are found at seven sites (labeled as X1, ..., X7), as shown in Fig. 5(e). These new sites are suitable for deuterium atoms. On the other hand, negative contours at the five independent D sites in ΔF maps are indicative for a depletion of deuterium atoms. Indeed, as their site occupancy parameters were refined without constraints, we obtained 0.96 at D4 and 0.98 at the other D sites. These observations are regarded as a result from dynamic disorder rather than static disorder because at elevated temperatures diffuse streaks became more

obviously between those new sites (X1, ..., X7) and the equilibrium D sites [Fig. 5(c)]. Hence, these seven X sites could be connected with the possible types of DDHBs (Fig. 2), as follows:

- (1) X1 at (0.5, 0, 0) is located in the middle of the 8MR-channel between two D4 sites in an equal distance of $d(X1-D4) = 1.54$ Å. X1 is a cross-over point between each HB-chain pair and hence can be associated with the motion Type 7 [Figs. 2(a) and 2(b)].
- (2) X2 at (0.5, 0.5205, 0.0779) is distanced about 1.368 and 1.384 Å from D1 and D4, respectively. X4 at (0.4637, 0.1562, 0) is located 1.584 Å away from D1 and 1.849 Å from D4. Hence, X2 and X4 can be connected to dynamic disorder between D1 and D4. X3 at (0.5470, 0.1562, 0) is 0.770 Å close to D1 and 1.359 Å to D4. X3 reflects librations or rotations at D1 (Type 1). The largest angle change $\angle(O1 - D1 \cdots O8) = 3.6^\circ$ agrees with the geometrically flexible O1-D1 group against those containing double acceptor D4-O10-D5 and D1-O9-D3 groups, facilitating intrachain-exchanging processes over D1 [Fig. 2(a)]. Diffuse intensities centered at X2, X3, and X4 indicate intrachain DDHBs over D1 and D4 sites.
- (3) X5 at (0.5, 0.0182, 0.3802) may reflect the site-exchanging process between D4 and D5 within a D4-O10-D5 group with the respective distance 0.847 Å to D4, 1.420 Å to O10, and 1.712 Å to D5. This can be assigned to motion Type 2 in Fig. 2.
- (4) X6 at (0.5, 0.792, 0.25) is centered between two D4 of the semihelical HB pair [Figs. D3(a) and D3(c)]. Similarly, X7 at (0.5, 0.850, 0.75) lies between two D5 sites of the semihelical HB pair [Figs. D3(b) and (d)]. X6 and X7 correspond to the respective interchain-exchanging process via D4-D4 (Type 4) and via D5-D5 (Type 5). X6 and X7 are connected by diffuse streaks of which the center is located at (0.5, 0.0380, 0.25) in a distance of 1.346 Å to all D4 and D5 sites. This is a strong hint of an interchain-exchanging process via DDHBs involving D4 and D5 (Type 6, Fig. 2).

In addition, ΔF maps show three maxima found within 4MR-ring cages: Z1 at (0.25, 0.7116, 0.5381) is located between two D2-O9-D3 groups [Fig. 5(f)], and its peak intensity clearly increases from 350 K [Fig. 5(b)] to 400 K [Fig. 5(d)]. Interestingly, the related inter-ring-exchanging process seems to occur via another site Z3 at (0.25, 0.7658, 0.6052) near D2 and O3, forming the dynamic route D3-Z1-Z3-D2. This is related to high electron density residuals near

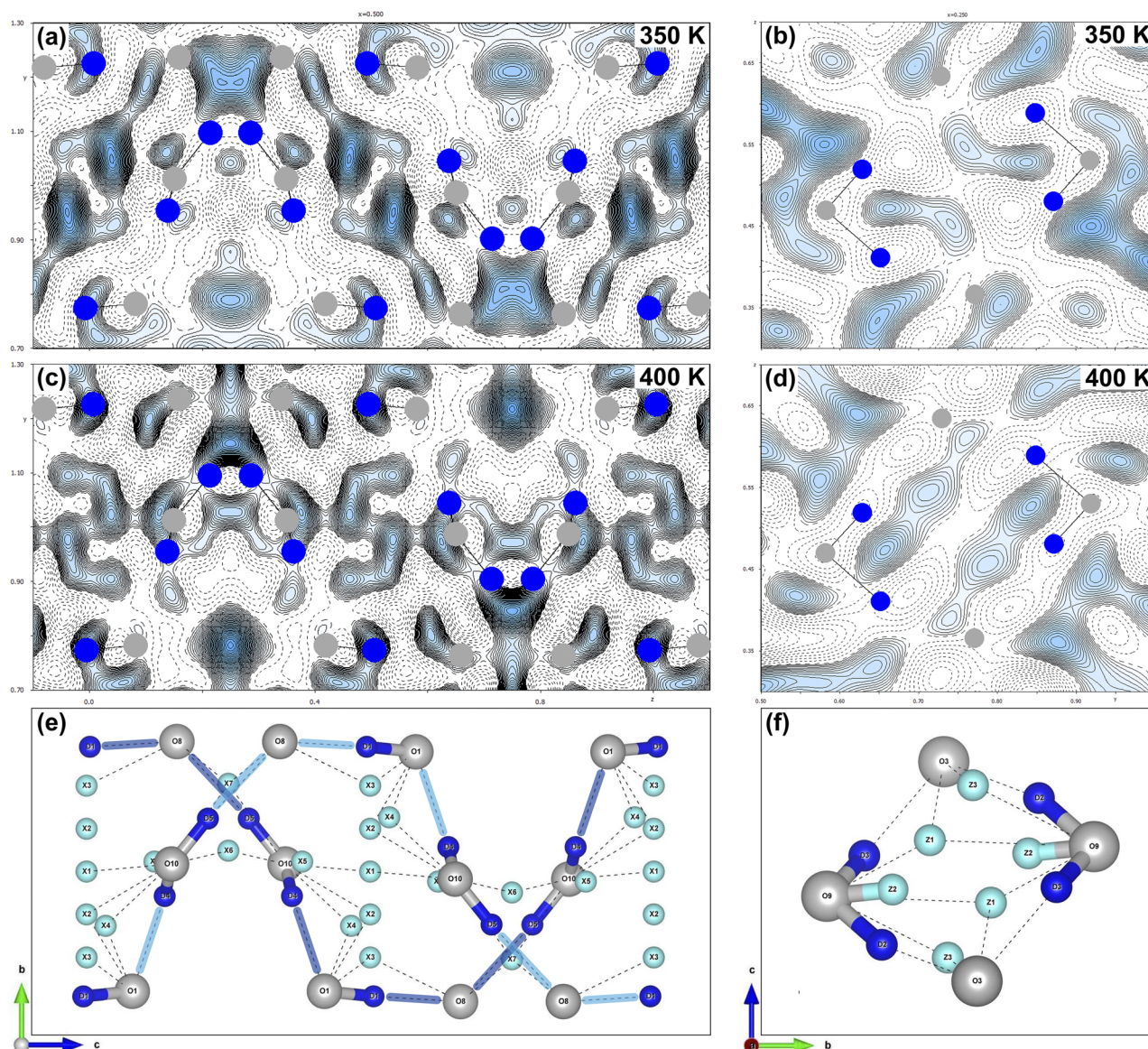


FIG. 5. ΔF maps of the Mn-hureaulite unit cell evaluated with HRNPD data at 350 K (a) and (b) and 400 K (c) and (d). ΔF slices are drawn for $x = 0.5$ from section ($0 \leq x \leq 1.0$; $0.7 \leq y \leq 1.3$; $-0.1 \leq z \leq 1.1$) [(a), (c), and (e)] and for $x = 0.25$ from section ($0.1 \leq x \leq 0.4$; $0.5 \leq y \leq 1.0$; $0.3 \leq z \leq 0.7$) [(b), (d), and (f)]. Positive densities are contoured by black lines and highlighted in blue, while negative densities are indicated by dotted lines. To guide the eyes, oxygen (light gray) and deuterium (blue) atoms in O1-D1, D2-O9-D3, and D4-O10-D5 groups are indicated. Diffuse elastic neutron scattering length densities are centered at seven possible deuterium sites (labeled as X1, ..., X7). As a result, several new HBs (broken lines) are rendered along the original semihelical HB chains highlighted in light and dark blue lines in (e) and (f).

O3 in ΔF maps evaluated with XSD above 300 K. Hence, Z1 and Z3 can be related to inter-ring-exchanges (Type 8). Z2 at (0.25, 0.6646, 0.4779) [Fig. 5(f)] originates from dynamic disorder between D2 and D3 of a D2-O9-D3 group (Type 3 in Fig. 2) and is associated with high electron density residuals around O9 in ΔF maps evaluated with XSD data (Fig. C.1).

The current neutron diffraction studies could resolve several new HBs of (X ... O ... X) in Fig. 5(e) and (Z ... O ... Z) in

Fig. 5(f), allowing to trace its DDHB-chains and DDHB-rings. These are significantly distorted with respect to the original HBs of Mn-hureaulite, as demonstrated by blue lines in Fig. 6(a). The new HBs feature no distinct sides of acceptor and donor oxygens for the presence of vivid DDHBs. The consequent distortion of DDHBs in this phosphatic oxyhydroxide framework is associated with a lowering in HB strengths and, more importantly, to the shortened distances for charge carriers (D), particularly between the semihelical HB chains,

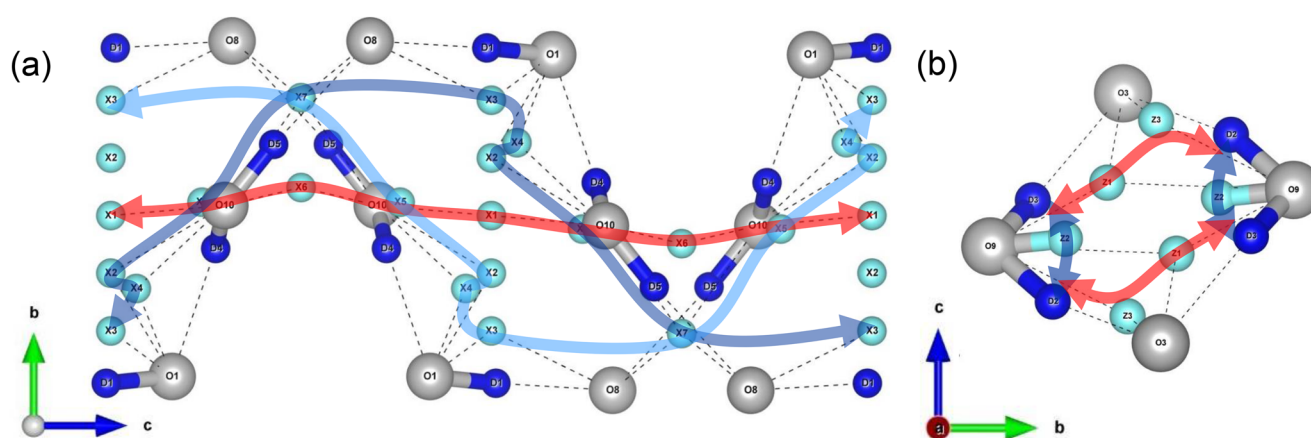


FIG. 6. Representative sections of semihelical HBs in deuterated Mn-hureaulite. The distortion of semihelical HB chain pairs highlighted by pale and dark blue lines can be realized in the presence of the new sites X1-X7 (a) and that of HB rings with Z1-Z3 (b). These rearrangements of HBs are due to DDHBs, by which new HBs connect to each other across the semihelical chain pair, as well as across the HB ring, indicated by thick red lines.

as highlighted by a red line in Fig. 6(a). This corresponds to the longest charge transport path across the semihelical HB-chain pair via D4-X1-D4 (Type 7), clearly seen through the 8MR pore opening [see Fig. D.4(c) of the [supplementary material](#)]. The neutron scattering density distribution around X1 is hardly recognizable at 350 K [Fig. D.4(a)], but quite obvious at 400 K [Fig. D.4(b)]. Hence, long-range charge transport may be realized once interchain-exchanging processes over the path D4-X1-D4 are thermally activated near 400 K.

The time scales of complex proton motions in Mn-hureaulite could be differentiated by QENS and DS, as described in Secs. III B and III C.

B. Fast proton motions seen in neutron spectroscopy

We observe quasielastic neutron scattering at FOCUS ($\Delta E = 45 \mu\text{eV}$) down to the lowest measurement temperature. The QENS signal barely changes below 250 K and can be assigned to paramagnetic scattering. Additional QENS intensity is observed at 300 and at 510 K, but surprisingly not in between (the data at 350 and 400 K are practically the same as those at 250 K). Figure E.1 of the [supplementary material](#) shows the difference spectra for the different temperatures. Based on these observations, we propose to eliminate the paramagnetic QENS signal by using the 250 K data as background. Detailed analysis reveals that at 300 K the QENS signal comes from water diffusion, presumably from surface-adsorbed water (see Sec. F of the [supplementary material](#)). At 350 K, the water diffusion is so fast that the broad QENS signal was not detected anymore. In the following, we focus on the QENS signal at 510 K, which can be associated with structural protons in Mn-hureaulite. The QENS spectrum at 510 K could be fitted with one Lorentzian function (Fig. 7),

$$I(Q, \omega) = \{A_{\text{elastic}}(Q) \delta(\hbar\omega) + A_{\text{QENS}}(Q) L(Q, \omega)\} \otimes R(Q, \omega). \quad (1)$$

The elastic line, $A_{\text{elastic}}(Q) \delta(\hbar\omega)$, has negative intensity because the more static state at 250 K resulted in an over-subtraction. The

amplitude $A_{\text{QENS}}(Q)$ incorporates both the structure factor of the mobile species and the intensity reduction at elevated temperatures due to thermal vibrations (Debye-Waller factor). The model function was convoluted with the resolution function measured by a vanadium standard, $R(Q, \omega)$.

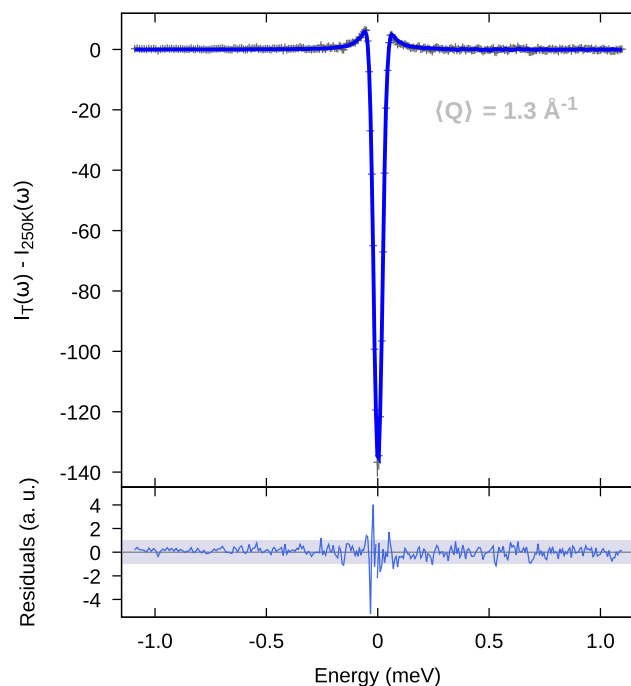


FIG. 7. Observed (+) and fitted (blue line) QENS spectra at 510 K for one representative Q-group. Their difference is shown at the bottom. Localized motions were described using one Lorentzian function (blue line).

The linewidth is Q -independent ($\Gamma \approx 0.08$ meV), and therefore, the QENS signal can be assigned to localized proton motions. Unfortunately, the Bragg peaks, the paramagnetic QENS contribution, and the small spectral weight of the localized motion hindered reliable evaluation of the elastic incoherent structure factor (EISF), which is commonly used to find the geometry of the motion. Therefore, we have performed a measurement at the IN16 backscattering spectrometer, which has a significantly better energy resolution ($\Delta E = 1$ μ eV).

The inelastic fixed window scan (IFWS) integrated with respect to Q (Fig. 8) exhibits one weak peak at $T_{\max} = 261$ K, which was assigned to the surface-adsorbed water. In addition, the IFWS shows a strong peak at $T_{\max} = 399$ K, which is Q -independent apart of the intensity (see Sec. F of the [supplementary material](#)), reinforcing that this relaxation stems from intrinsic local motions. The onset temperature for the local dynamics is close to 300 K, but still present at the highest measuring temperature of 483 K. Accordingly, this local dynamic process is the same as the one measured at 510 K at FOCUS (Fig. 7).

The Q -integrated IFWS spectra were fitted to obtain the relaxation time as a function of temperature according to Frick *et al.*,⁴⁶

$$I_{IFWS}(T) = C + A_{bw}L_{bw}(T, \Gamma_{bw}(T)) + A_{loc}L_{loc}(T, \Gamma_{loc}(T)), \quad (2)$$

where $\Gamma(T)$ is the width of the Lorentzian function [see, e.g., Eq. (1)], and C is a constant background. The peak intensity is related to the number of protons participating in the motion. We note that this model is only a crude approximation for the water diffusion

with Q -dependent $\Gamma_{bw}(T)$, but it can satisfactorily reproduce the bump caused by the surface water. Using a simple Arrhenius-type model, we obtain $\Gamma_{loc}(T = 510 \text{ K}) = 0.070(2)$ meV, which is in reasonably good agreement with the value from FOCUS (~ 0.08 meV). The corresponding relaxation time is 110(17) ps at 399 K. The activation energy was found to be $E_a = 0.390(4)$ eV for the local dynamics.

Fixing $\Gamma_{loc}(T)$ to the above-obtained Arrhenius function, the measurement statistics of the IFWS allowed a Q -dependent fit with the simplified expression [Eq. (3)], where the surface water contribution was hidden by the statistical fluctuations, and so it could be neglected,

$$I_{IFWS}(Q, T) \propto \frac{\pi}{B} A_1(Q) \frac{\tau(T)}{1 + \omega_{off}^2 \tau(T)^2}, \quad (3)$$

where $A_1(Q)$ is the temperature-independent inelastic incoherent structure factor (IISF)⁴⁷ and $\omega_{off} = 3$ μ eV is the energy offset of the IFWS. The Debye–Waller factor B did not change significantly in the limited temperature range of the IFWS peak. The simplest model for the local diffusion process, which complies with the previous structural observations, is the two-site jump model,⁴⁸

$$A_1(Q) = \frac{1}{2} (1 - j_0(Qd)), \quad (4)$$

where we have approximated the first order Bessel function with $j_0(Qd) = \sin(Qd)/(Qd)$. $A_1(Q)$ was fitted well (Fig. 9) for a particle motion between two positions separated by the jump distance $d = 1.70(7)$ Å (Fig. 9).

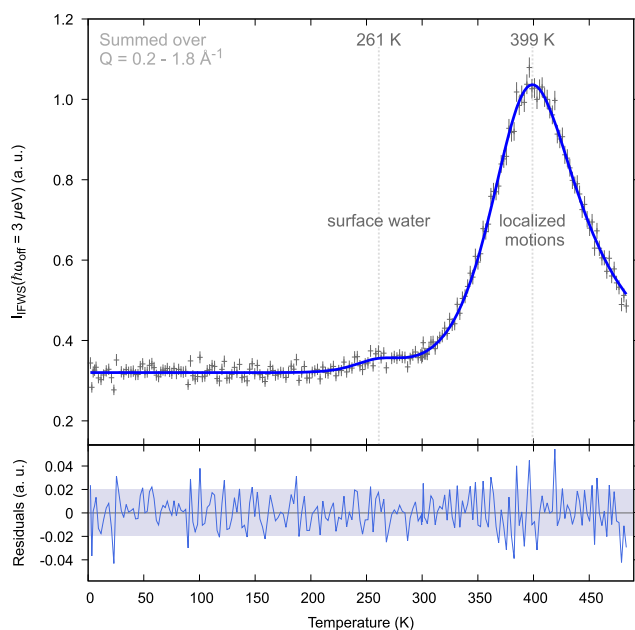


FIG. 8. IFWS data fit using a linear background and the Arrhenius relation for both observed relaxations. Their peak temperatures are highlighted by the gray dashed lines. I_{IFWS} data were summed over the measured Q -range.

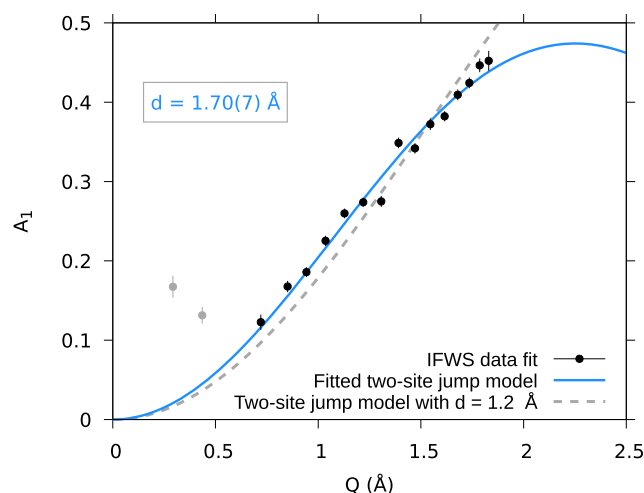


FIG. 9. Fitted quasielastic incoherent structure factor A_1 obtained from IFWS Arrhenius fits of the local relaxation peak. Black dots represent the A_1 values taken into consideration in the two-site model fit, which resulted in a jump distance of $1.70(7)$ Å. The corresponding fit ($A_1 = 0.337(15) \times [1 - j_0(Q \times 1.7)]$) is drawn in blue. For comparison, the gray, dashed line gives the two-site model function with $d = 1.2$ Å, a typical proton-to-proton-donor distance (see Table II).

These local hydrogen motions can be assigned to specific proton sites in Mn-hureaulite. We elaborate first the number of participating H atoms based on the IISF,

$$\frac{I_{\text{mobile}}}{I_{\text{mobile}} + I_{\text{static}}} = \frac{I_{\text{QENS}}}{A_1(I_{\text{QENS}} + I_{\text{elastic}})} \quad (5)$$

The mean value for A_1 was calculated by integration of Eq. (4) over $0.55 \leq Q \leq 1.45 \text{ \AA}^{-1}$. We find $I_{\text{mobile}}/(I_{\text{mobile}} + I_{\text{static}}) \approx 0.4$, which means that two out of the five different protons are participating in this localized motion. Most obviously, a site exchange could happen within an H–O–H group. Nevertheless, we have examined all possible jump distances, including interstitial positions. The direct distance $1.633(8) \text{ \AA}$ between D4 and D5 in a D4–O10–D5 group and $1.577(6) \text{ \AA}$ between D2 and D3 in D2–O9–D3 at 400 K (Table II) is comparable to the jump distance of $1.70(7) \text{ \AA}$ (Fig. 9). Considering that the APDs at D4 and D5 sites are much larger than those at D2 and D3 in the relevant temperature range (Fig. 4 and insights from simulations, Sec. III D), the site-exchanging proton

pair within H4–O10–H5 is regarded as the main contributor to the localized jump dynamics.

C. Dielectric behavior of protonated and deuterated Mn-hureaulite

Figure 10 shows the temperature dependence of the dielectric constant, ϵ' , and the real part of the conductivity, σ' , plotted for various frequencies. Frames (a) and (c) present the results for the protonated and frames (b) and (d) for the deuterated hureaulite. The protonated system was measured in an extended frequency and temperature range. It should be noted that σ' and the dielectric loss ϵ'' are related via $\sigma' \propto \epsilon''\nu$. Therefore, the $\sigma'(T)$ curves in Figs. 10(c) and 10(d) exhibit the same temperature dependence as ϵ'' (irrespective of different absolute values).

ϵ' of both systems [Figs. 10(a) and 10(b)] significantly increases with increasing temperature above about 300 K (H-form) or 275 K (D-form). The shoulders seen in both cases and their shift to higher temperatures for higher measurement frequencies indicate

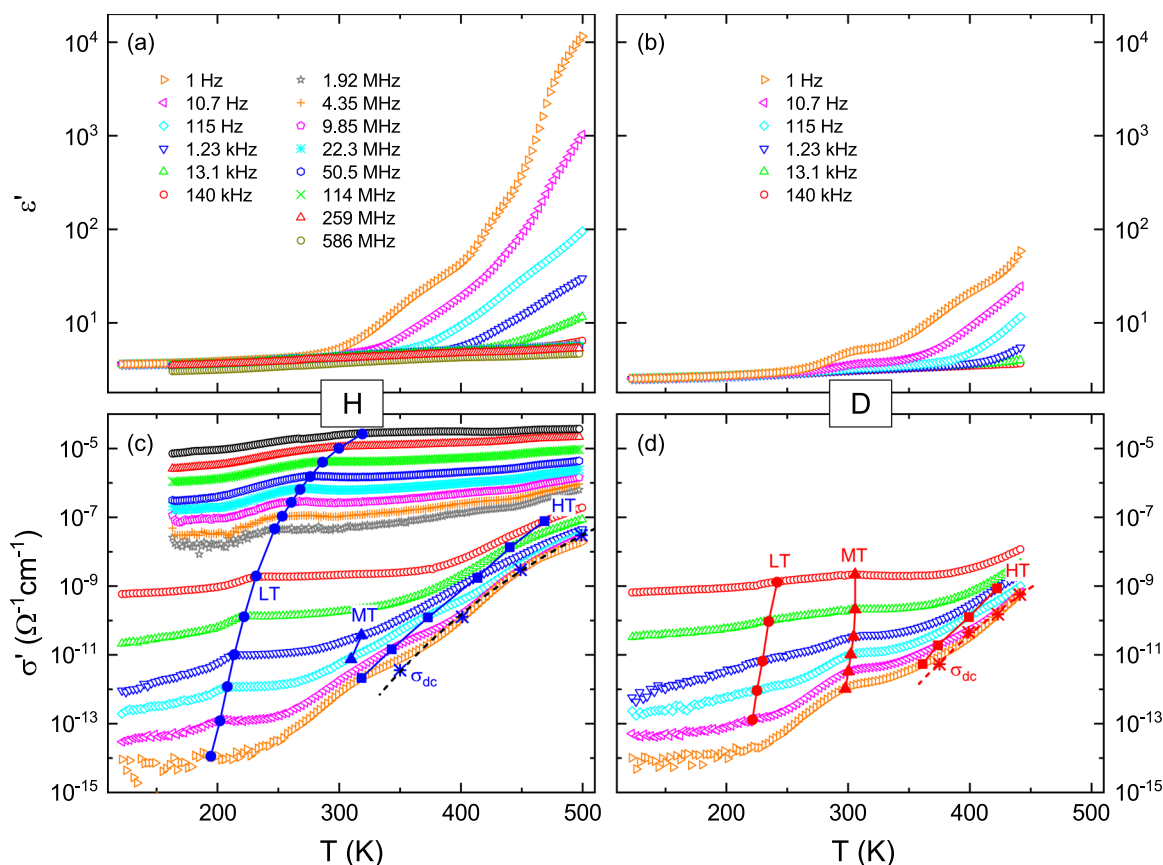


FIG. 10. $\epsilon'(T)$ and $\sigma'(T)$ of protonated (H) [(a) and (c)] and deuterated (D) [(b) and (d)] Mn-hureaulite, shown for various frequencies. The filled circle, triangle, and square symbols mark the respective LT-, MT-, and HT-relaxation modes. The solid lines are guides for the eye. The stars indicate the dc conductivity as obtained from fits of the dielectric spectra, as shown in Fig. H.1. The dashed lines are Arrhenius fits of $\sigma_{\text{dc}}(T)$. Note that the imaginary part of the permittivity $\epsilon''(T)$ is not shown here since it is simply proportional to the real part of the conductivity via $\sigma' = 2\pi\nu\epsilon''\epsilon_0$. Degradation of the thin deuterated sample pellet limited the data acquisitions to a maximum of 450 K.

a relaxational origin of this behavior.^{49,50} At elevated temperatures and low frequencies, $\epsilon'(T)$ approaches high values, even becoming “colossal”⁵¹ (>1000) for the protonated sample. This indicates that this part of the dielectric response is of non-intrinsic nature and probably due to electrode polarization. Such effects, sometimes termed “blocking electrodes,” are often found for ionic conductors and arise when the conducting ions are blocked at the electrodes to form space-charge regions acting as large capacitors.⁵²

The temperature-dependent conductivity σ' , shown in Figs. 10(c) and 10(d), reveals several peaks or shoulders, whose positions are indicated by the filled symbols. They shift to higher temperatures with increasing frequency, again pointing to a relaxational origin.^{49,50} For both materials, three intrinsic relaxation processes show up the following:

- (1) The protonated material [Fig. 10(c)] reveals a well-defined low-temperature (LT) relaxation mode at temperatures between about 180 and 300 K. A corresponding, but less pronounced LT mode is also found for the deuterated sample [Fig. 10(d)] at temperatures about 30 K higher for identical frequencies. The estimated peak positions of these relaxations are indicated by the filled circles in Figs. 10(c) and 10(d).
- (2) A middle-temperature (MT) relaxation mode at around 300 K is clearly resolved in the D-form but barely visible in the H-form [filled triangles in Figs. 10(c) and 10(d)]; a weak shoulder seen, e.g., around 400 K for the 1.9 MHz curve of the H-form may also be due to this relaxation]. The temperature of the MT-mode peak is only weakly frequency-dependent.
- (3) A strongly frequency-dependent HT-relaxation above 300 K is found in both systems [filled squares in Figs. 10(c) and 10(d)]. It only shows up as a shoulder because it is strongly superimposed by an additional increase of $\sigma'(T)$ at higher temperatures, which is due to dc conductivity (see discussion at the end of this section). For 1 Hz, the HT-mode appears at ~ 360 K in the D-form, while it shows up at about 320 K in the H-form.

In principle, each of these relaxation features in $\sigma'(T)$ should be accompanied by a step-like increase (with increasing T) in $\epsilon'(T)$. This indeed is the case for the HT relaxation in the protonated sample and for the MT and HT relaxations in the deuterated one [Figs. 10(a) and 10(b)]. The relaxation steps of the other processes are too small to be detected. For the protonated sample, it should be noted that the indicated peaks or shoulders in Fig. 10(c) show up at temperatures and frequencies that are far off the region where the colossal ϵ' values are observed in Fig. 10(a). This is in accord with an intrinsic nature of the corresponding relaxation processes.^{51,52}

As discussed in Sec. H of the [supplementary material](#), the three detected relaxation processes are difficult to deconvolute in the frequency-dependent plots of the dielectric quantities. Therefore, we rely on the temperature-dependent graphs of Figs. 10(c) and 10(d) to determine the corresponding relaxation times. In general, for a fixed measurement frequency ν , a peak in $\sigma'(T)$ [or in $\epsilon''(T)$] occurs when the temperature-dependent relaxation time $\tau(T)$ matches the condition $\tau(T) = 1/(2\pi\nu) = 1/\omega$. Thus, from the peak temperatures in the $\sigma'(T)$ plots of Figs. 10(c) and 10(d), we can deduce the temperature-dependent relaxation times. Figure 11

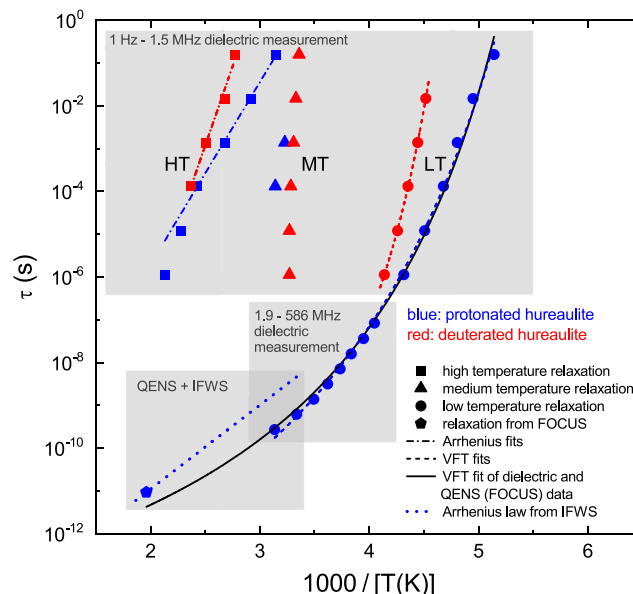


FIG. 11. Arrhenius representation of the relaxation times of the LT, MT, and HT relaxations as deduced from temperature-dependent σ' plots (Fig. 10) for the protonated (blue) and deuterated (red) Mn-hureaulite. In addition, results from neutron scattering are shown (pentagon: QENS using FOCUS; blue dotted line: IFWS using IN16B). The dashed-dotted lines are Arrhenius fits of the HT data (parameters: see text). The dashed lines are fits of the LT relaxation times from DS with the VFT equation [Eq. (6)]. The solid line shows a VFT fit of the combined DS (blue circles) and FOCUS data (pentagon) of the H-form with Eq. (6). The parameters of the VFT fits are given in Table III. The gray boxes highlight from which type of measurements the data points originate.

presents the obtained $\tau(T)$ results for all relaxation modes and both materials using an Arrhenius representation. The τ values determined for the HT modes (squares) can be reasonably well fitted by an Arrhenius law, $\tau = \tau_0 \exp[E/(k_B T)]$ (dashed-dotted lines), with some deviations for the two highest temperatures of the H-form. We obtain energy barriers E of 0.84 and 1.5 eV for the H- and D-forms, respectively. The pre-exponential factor τ_0 can be assumed to be related to the inverse of the attempt frequency of the corresponding thermally activated motion via $\nu_0 = 1/(2\pi\tau_0)$, which, usually, is in the phonon-frequency range for canonical relaxations. We find $\tau_0 \approx 6 \times 10^{-15}$ s and 4×10^{-22} s for the protonated and deuterated samples, respectively. Especially for the latter, τ_0 seems unreasonably low. Such discrepancies may indicate deviations from Arrhenius behavior, which are not resolved here due to the limited frequency and temperature region where the HT relaxation could be observed.

However, for the LT modes (circles in Fig. 11), such non-Arrhenius behavior of $\tau(T)$ could be clearly detected, especially for the H-form, which was measured in an extended frequency region up to several hundred MHz. Its $\tau(1/T)$ curve (blue circles) exhibits clear bending, characteristic for the glassy freezing of relaxational dynamics.^{49,53,54} Such behavior is usually described by the empirical Vogel-Fulcher-Tammann (VFT) equation^{53,55,56}

$$\tau = \tau_0 \exp\left(\frac{DT_{VF}}{T - T_{VF}}\right). \quad (6)$$

Here, D is the so-called strength parameter, providing a measure of the deviations from the Arrhenius behavior.^{55,56} T_{VF} is the Vogel–Fulcher temperature, at which the relaxation time would diverge. Indeed, a good fit of the experimental LT data for the H-form is achieved in this way (dashed blue line in Fig. 11). A close look at the $\tau(1/T)$ data of the LT relaxation of the D-form (red circles) reveals a curved behavior for this sample, too, and these data could also be well fitted by Eq. (6) (dashed red line).

For the protonated Mn-hureaulite, $\tau(T)$ of the dielectric LT-relaxation seems to be rather well consistent with τ of the localized relaxation, detected by QENS using the FOCUS spectrometer (pentagon in Fig. 11). The black solid line in Fig. 11 shows a VFT fit of the combined FOCUS and DS relaxation-time data. While some deviations of fit and experimental data show up at high temperatures, the agreement is satisfactory, having in mind that two completely different experimental methods were used. In this context, it should also be noted that inelastic neutron scattering essentially detects density fluctuations, while dielectric spectroscopy is sensitive to dipolar fluctuations only. Thus, the small mismatch between the relaxation times from the two methods, suggested by the VFT fit in Fig. 11, in principle, could indicate a weak decoupling of both dynamics. In general, such decoupling effects, leading to the detection of different relaxation times by DS, neutron scattering, and other spectroscopic methods, are rather well known, especially in glass physics,^{54,57,58} and some theoretical explanations were provided.^{59,60}

The VFT parameters, as obtained from the fits of the LT relaxation times, are listed in Table III. In all cases, the VFT fits gave rise to reasonable inverse attempt frequencies τ_0 . The strength parameters between 6.8 and 13.0 classify these materials as fragile to intermediate within the strong/fragile classification scheme proposed by Angell.^{55,56} The obtained T_{VF} values point to an isotope effect of the relaxation dynamics: The Vogel–Fulcher temperature for the D-form is significantly higher than for the H-form sample (for both evaluations of the latter). Obviously, the deuterium dynamics slows down more strongly upon cooling, leading to much higher τ values in the investigated temperature range as directly revealed in Fig. 11. Based on the reasonable match of the DS and QENS relaxation-time data, the LT-mode can be assigned to site exchanging H4 and H5 (or D4, D5) in the H4–O10–H5 (or D4–O10–D5) groups [Type 2 in Fig. 2(a)]. This local proton-hopping process obviously exhibits glassy freezing, and, similar to the findings in our previous work on a rockbridgeite-type compound,⁶¹ Mn-hureaulite approaches a “proton glass” state^{62,63} at low temperatures. The corresponding glass-transition temperature T_g can be deduced by applying the usual criterion $\tau(T_g) = 100$ s.⁵⁴ This leads to $T_g = 187$ and 212 K for the H- and D-form, respectively, implying that the deuterium dynamics freezes at higher temperature.

TABLE III. Parameters obtained by fitting $\tau(T)$ of the LT relaxation (Fig. 11) using the VFT law [Eq. (6)].

	D	T_{VF}	τ_0 (s)
H-form, DS	13.0	137	9.7×10^{-15}
H-form, DS + QENS	9.5	147	9.2×10^{-14}
D-form, DS	6.8	179	3.2×10^{-15}

The MT mode (triangles in Fig. 11), for which significant $\tau(T)$ data are only available for the D-form, can, in principle, also be described by an Arrhenius law. However, due to the very weak temperature dependence of its relaxation time, the inverse attempt frequency τ_0 (the y-axis intercept in the Arrhenius plot in Fig. 11) would be unreasonably low, rendering such a fit meaningless. More likely, strong deviations from Arrhenius behavior exist for this relaxation at higher temperatures that are not resolved due to the limited temperature range where this mode could be detected. Considering the similar ADP values at all D sites up to 300 K (Fig. 4), one may tentatively assign the MT-relaxational motions, resolved in the DS data near 300 K, to superimposed fast librations of dangling OH and HOH groups. The HT-mode, treated above, may be assigned to inter- and intrachain-exchanges involving H4 (or D4) sites. This is in agreement with the increased ADP eigenvalue $U_3(D4)$, which is significantly higher than $U_3(D1)$ in the same temperature interval from 350 to 400 K (Fig. 4).

Finally, the present dielectric data also provide information on the dc conductivity of Mn-hureaulite. As discussed in Sec. H of the [supplementary material](#), it shows up as a plateau in the $\sigma'(\nu)$ plots and can be derived from fits of the dielectric spectra. Here, it is essential to account for the electrode contributions at low frequencies by an equivalent-circuit approach as discussed in detail, e.g., in Refs. 51 and 52. The resulting dc conductivities for four temperatures are shown by the stars in Figs. 10(c) and 10(d). They are well consistent with the $\sigma'(T)$ results at the lowest frequencies. The moderate absolute values of $\sigma_{dc}(T)$ indicate that Mn-hureaulite is not a superprotonic conductor. As shown by the dashed lines, these data can be reasonably well-fitted by an Arrhenius law, $\sigma_{dc}(T) \propto \exp[-E/(k_B T)]$. We obtain practically identical energy barriers for both systems, namely, $E = 0.92$ eV for the H-form and $E = 0.97$ eV for the D-form.

D. DDHBs associated with the lattice dynamics

Polyhedral rotations of structural building units readily occur from a certain degree of distortion in releasing intra-polyhedral and inter-polyhedral strains.⁶⁴ In Mn-hureaulite, three unique manganese octahedra $Mn1O_6$, $Mn2O_4(HOH)_2$, and $Mn3O_5(HOH)$ are edge-sharing to build the highly distorted pentamer unit established by the $Mn2$ – $Mn3$ – $Mn1$ – $Mn3$ – $Mn2$ atomic sites.^{14,15} Thus, all hydrogen motions might be coupled to bending motions of $Mn1O_6$, $Mn2O_4(HOH)_2$, and $Mn3O_5(HOH)$. We expect an immediate impact of these motions both on the local re-orientations and the long-range proton diffusion through the temporal alteration of the potential energy landscape.

Now let us consider the INS part of our neutron scattering spectra (Fig. 12). INS spectra are dominated by hydrogen vibrations due to their dominant neutron scattering length. We obtain a very good agreement of the density of states (DOS) between calculation and measurement even though only the subset of hydrogen atoms are evaluated (Fig. 13). Unfortunately, the non-linear transformation of measured intensity from the flight time to the energy scale made some spectral features less visible. Therefore, we plot the temperature dependence of the spectrum as time-of-flight data, corrected by the Bose–Einstein occupation factor (Fig. 12).

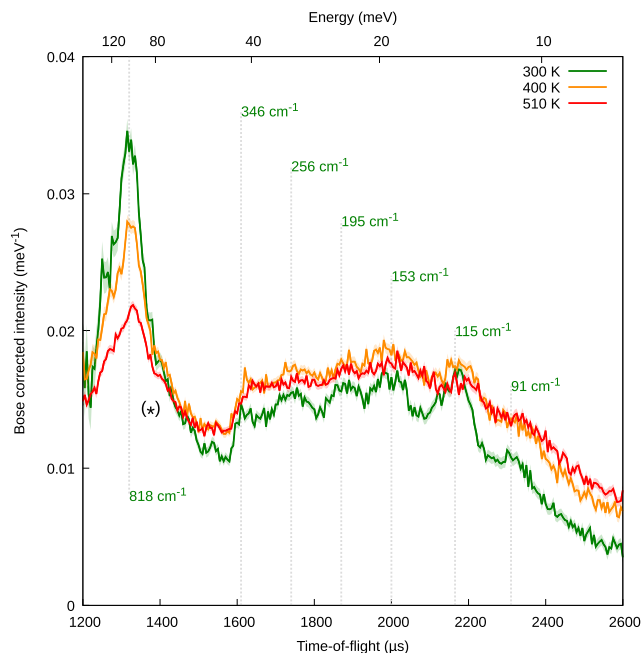


FIG. 12. Bose-corrected INS intensity summed over all detectors for each measuring temperature is shown within the flight time range. The black asterisk (*) marks a higher order spurion. The transparent bands represent the error of a measurement.

The most dominant peak in the INS spectrum at 300 K is located near 818 cm^{-1} (or 101 meV), as shown in Figs. 12 and 13. From simulated Raman spectra,⁶⁵ the wavenumber region near 818 cm^{-1} refers to the HOH libration modes of $\text{Mn}_2\text{O}_4(\text{HOH})_2$ octahedra [i.e., a rocking (in-plane) mode, $\rho(\text{H4-O10-H5})$; a twisting (out-of-plane) mode, $\omega(\text{H4-O10-H5})$]. In addition, these modes are superimposed by the librations of HOH ligand groups of $\text{Mn}_3\text{O}_5(\text{HOH})$ octahedra and $\text{P1O}_3(\text{OH})$ tetrahedra [i.e.,

$\omega(\text{H2-O9-H3})$; a wagging (out-of-plane) mode, $\tau(\text{H2-O9-H3})$; an out-of-plane-bending mode, $\gamma(\text{P1-O1-H1})$]. On the other hand, the low energy range below 400 cm^{-1} is assigned to bending motions of Mn1O_6 , $\text{M2nO}_4(\text{HOH})_2$, and $\text{Mn3O}_5(\text{HOH})$ octahedra.

The main reason for the decreasing peak intensity near 818 cm^{-1} in INS spectra at elevated temperatures could be addressed to redistribution of motions of HOH and OH group. Above 300 K, the enhanced collective motions of framework polyhedra are supported by strongly smeared INS peaks below 400 cm^{-1} (Fig. 12). Considering the light-weighted H species, their motions can be enhanced by collective motions of the framework polyhedra, rather than the other way around.

Finally, we support the interpretation of previous experimental data by simulations. Based on the AIMD trajectories, the mean square displacement (MSD) and the spatial density distribution (sdf) for each characteristic proton site were analyzed at different temperatures (Fig. 14). In accordance with ADP values determined by Rietveld analyses with HRNPD data, the increasing MSD of H4 with temperature clearly exceeds the MSD of other protons. The overlapping sdf of H4 with that at H5 having the second largest MSD [Fig. 14(a)] could unambiguously confirm the assignment of QENS signal and the LT-relaxation mode resolved in σ' spectra near 300 K to fast reorientational motions within H4-O10-H5. We would like to note here that the duration of the simulation is short in comparison to the experimental relaxation times. Therefore, it is not surprising that we do not directly observe the diffusional motions in the simulations.

In the sdf plots from 300 K up to 500 K, the interchain site-exchanges over H4 along with H5 are strongly enhanced at 500 K [Fig. 14(g)]. However, the inter-ring site-exchanges of (H2-O9-H3) pairs [Fig. 14(h)] are less promoted even at 500 K than the interchain-exchanging case. Hence, the HT-relaxation mode in Fig. 10 is related to interchain-exchanges. Furthermore, in Fig. 14(g), it is easy to recognize a strong overlapping of the spatial density distribution in H4-X1-H4, the pathway suggested for the protonic conductivity in Mn-hureaulite, as described in Sec. III A.

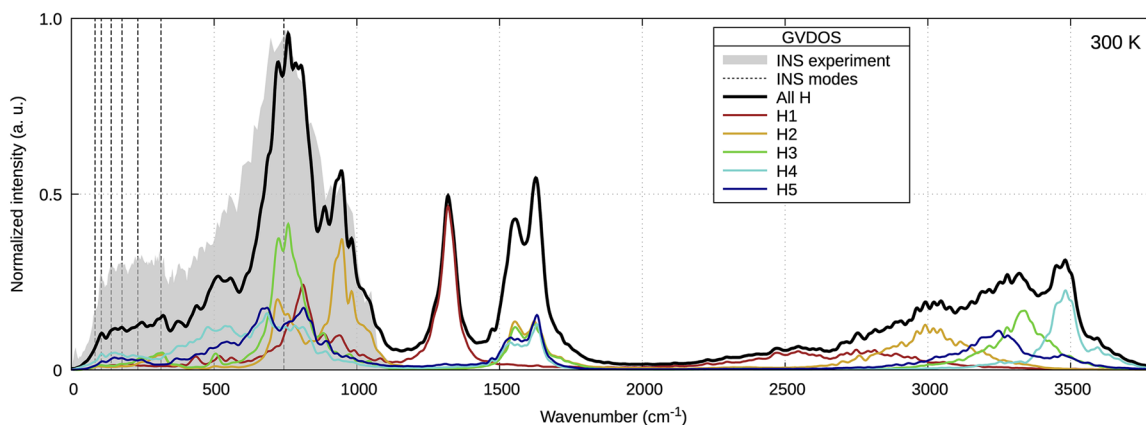


FIG. 13. GVDOS from observed INS spectra (gray) and simulated partial DOS for five sites for the five hydrogen sites in Mn-hureaulite at 300 K. The frequency of the experimental GVDOS was multiplied by a scaling factor of 0.95. The dashed lines highlight the vibrational modes found with INS (Fig. 12). The simulated DOS is calculated from CP2K NVE trajectories.

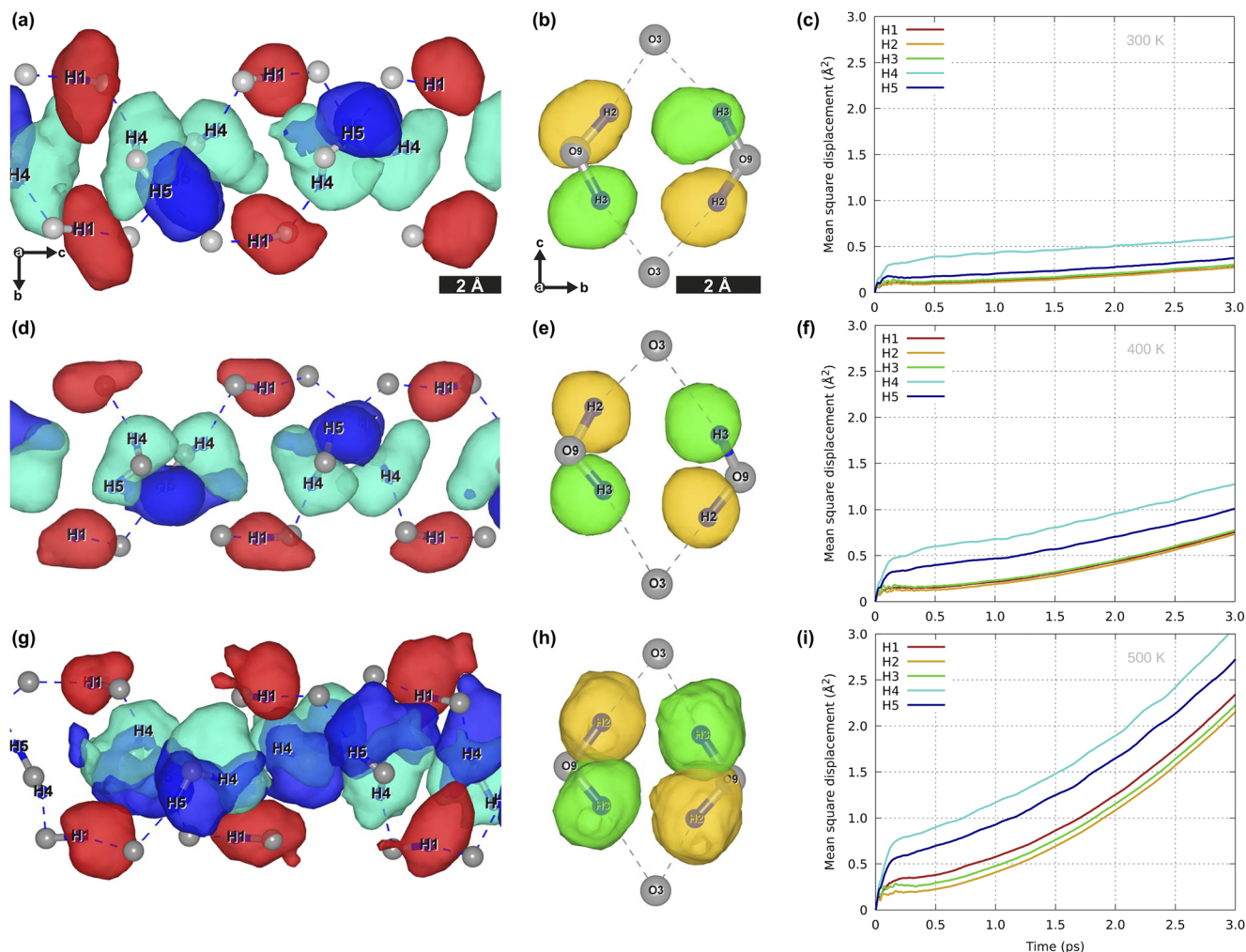


FIG. 14. Temperature evolution of spatial density distribution functions (left and middle column) and mean square displacements (right column) of the characteristic proton sites. Small sections of HB chains [(a), (d), and (g)] and rings [(b), (e), and (h)] plotted here. Both sections include the spatial density distributions around the proton sites. T -dependent mean square displacements at all five proton sites from NVE trajectories are drawn on the right [(c), (f), and (i)].

IV. CONCLUSION

Detailed inspection of difference Fourier maps from HRNPD data indicates the following dynamics for the five unique deuterium sites in Mn-hureaulite:

- (1) Deuterium at D1 in O1-D1 is fast rotating along a semi-helical HB chain above 350 K. This motion can contribute to intrachain-exchanging processes.
- (2) D2 and D3 in D2-O9-D3 are confined by a 4MR-opening. Deuterium atoms at both sites show fast re-orientations up to 350 K. At 400 K, inter-ring-exchanging processes start across each HB ring.
- (3) Deuterium atoms at D4 and D5 in D4-O10-D5 show largest dynamic disorder along the 8MR-channel system, which is relevant for both intra- and interchain-exchanges.

The most interesting finding in the HRNPD data analyses is the pathway D4-X1-D4, highlighted in red in Fig. 6(a). This interchain-exchange enables thermally activated long-range charge transport by DDHB-chains along the c axis. The efficiency of proton transport between semihelical chains is limited by relatively large proton-to-proton-donor distances. This reflects a magnitude of 10^{-7} S/cm for the dc conductivity in the H-form at 500 K [Fig. 10(c)].

In addition, fast site-exchanges of the two protons in H4-O10-H5 (along with fast reorientation of H1) is a relevant prerequisite for intrachain charge transport. QENS evinced local dynamics corresponding to a two-site jump model characterized by an activation energy of 0.390(4) eV and relaxation time of 110(17) ps at 399 K with a jump distance of 1.70(7) Å. AIMD results agreed with the jump model for site-exchanging H4 and H5 in a H4-O10-H5

group even if the simulation time was too short to observe an explicit site-exchange. This local site-exchanging process showing non-Arrhenius behavior could be assigned to the LT-relaxational mode detected in dielectric spectroscopy. This dynamics exhibits clear signatures of glassy freezing, and, finally, a proton-glass state is approached at 187 K.

In conclusion, the long-range charge transport in Mn-hureaulite is realized by DDHB-chains. The thermal response of the framework structure ensures the anisotropically widened channel opening at elevated temperatures for the ease of DDHBs with dangling HOH and OH groups. This, in turn, requires collective motions of the octahedral-tetrahedral framework, particularly of $\text{Mn}_2\text{O}_4(\text{HOH})_2$ octahedra and $\text{P}_1\text{O}_3(\text{OH})$ tetrahedra with the respective H4–O10–H5 and O1–H1 dangling groups. In addition, both framework polyhedral moieties frame the pore opening of the 8MR-channel system. The low energy bending modes of $\text{Mn}_2\text{O}_4(\text{HOH})_2$ octahedra below 400 cm^{-1} are strongly smeared out from 300 to 400 K. These are directly related to a strong intensity decrease of the dominant INS peak near 818 cm^{-1} associated with $\rho(\text{H4-O10-H5})$ and $\omega(\text{H4-O10-H5})$ modes. This points to a narrow interplay between phonons and proton dynamic disorder in the title compound. The temperature evaluation of sdf calculations could confirm a significant contribution of interchain-exchanging protons over the longest pathway H4–H4 (Type 7) to the protonic conductivity. From 300 K up to 500 K, the most profound increase of mean square displacements was found at H4 by AIMD calculations in accord with results from neutron powder diffraction.

Despite the absence of superprotonic conductivity in Mn-hureaulite, the current study could comprehend subtle motions at five independent H/D sites by providing their length and time scales in the highly complex, dynamically disordered HB network. Upon this success, further investigation on various types of DDHBs are continued to achieve superprotonic conductivity under mild external fields.

SUPPLEMENTARY MATERIAL

See the [supplementary material](#) for more details on structure refinements, QENS measurements, DFT computations, and frequency-dependent dielectric data. The supplementary movie visualizes proton motions at elevated temperatures. The mp4 file was created from the NpT AIMD trajectories at 500 K.

ACKNOWLEDGMENTS

This work was supported by a grant from the Swiss National Supercomputing Centre (CSCS) under Project No. s951 and from PSI's share at CSCS with Project No. psi01. Our study is partially based on experiments performed at the Swiss Spallation Neutron Source SINQ, Paul Scherrer Institut, Villigen, Switzerland. Other parts of this research were carried out at beamline P24 at PETRA III (DESY, Hamburg, Germany), a member of the Helmholtz Association HGF. A.H. was funded by an Erasmus + scholarship in the framework of MaMaSELF, provided by the EACEA, and thanks the Leibniz Supercomputing Centre (LRZ) of the Bavarian Academy of Sciences and Humanities (BAdW) for the provisioning and support of computational resources.

AUTHOR DECLARATIONS

Conflict of Interest

We have no conflicts of interest to disclose.

Author Contributions

S.-H.P. designed the current study and was responsible for beamtime applications for synchrotron x-ray diffraction and neutron scattering. All authors contributed equally to investigations done in this study with their disciplines. The manuscript was written by S.-H.P., A.H., P.L., F.J., and M.K. and edited by all authors. The supplementary material was prepared mainly by A.H.

DATA AVAILABILITY

The data that support the findings of this study are available within the article and its [supplementary material](#). Raw data were generated at the DESY, PSI, and ILL large scale facilities. Derived data supporting the findings of this study are available from the corresponding author upon reasonable request.

NOMENCLATURE

8MR	8-membered ring
ADP	atomic displacement parameter
AIMD	<i>ab initio</i> molecular dynamics
bw	bulk water
CP2K	name of the used DFT program
D	deuterium
DDHB	dynamically disordered hydrogen bond
DFT	density functional theory
DOS	density of states
DS	dielectric spectroscopy
EISF	elastic incoherent structure factor
FOCUS	neutron time-of-flight spectrometer at SINQ, PSI
FWS	fixed window scan
GoF	goodness of fit
GVDOS	generalized vibrational density of states
H	hydrogen
HB	hydrogen bond
HF	high frequency
HRNPD	high-resolution neutron powder diffraction
HT	high-temperature
IFWS	inelastic fixed window scan
IISF	inelastic incoherent structure factor
IN16B	neutron backscattering spectrometer at ILL
INS	inelastic neutron scattering
LF	low frequency
loc	localized
LT	low-temperature
MD	molecular dynamics
Mn-hureaulite	$\text{Mn}_5[(\text{PO}_4)_2(\text{PO}_3(\text{OH}))_2](\text{HOH})_4$
MSD	mean square displacement
MT	middle-temperature
NVE	microcanonical ensemble
NVT	canonical ensemble
QENS	quasielastic neutron scattering

sdf density distribution function
VFT Vogel–Fulcher–Tammann
XSD x-ray single crystal diffraction
ΔF difference Fourier

REFERENCES

- ¹Q. Chen and A. Braun, “Protons and the hydrogen economy,” *MRS Energy Sustainability* **4**, 14 (2017).
- ²A. Borgschulte, J. Terreni, E. Billeter, L. Daemen, Y. Cheng, A. Pandey, Z. Łodziana, R. J. Hemley, and A. J. Ramirez-Cuesta, “Inelastic neutron scattering evidence for anomalous H–H distances in metal hydrides,” *Proc. Natl. Acad. Sci. U. S. A.* **117**, 4021–4026 (2020).
- ³S. Tao, L. Zhai, A. D. Dinga Wonanke, M. A. Addicoat, Q. Jiang, and D. Jiang, “Confining H₃PO₄ network in covalent organic frameworks enables proton super flow,” *Nat. Commun.* **11**, 1981 (2020).
- ⁴S. M. Haile, D. A. Boysen, C. R. I. Chisholm, and R. B. Merle, “Solid acids as fuel cell electrolytes,” *Nature* **410**, 910–913 (2001).
- ⁵*Proton Conductors: Solids, Membranes, and Gels-Materials and Devices*, edited by P. Colomban (Cambridge University Press, New York, 1992), pp. 175–234.
- ⁶P. Colomban, “Proton conductors and their applications: A tentative historical overview of the early researches,” *Solid State Ionics* **334**, 125–144 (2019).
- ⁷A.-C. Dupuis, “Proton exchange membranes for fuel cells operated at medium temperatures: Materials and experimental techniques,” *Prog. Mater. Sci.* **56**, 289–327 (2011).
- ⁸A. I. Baranov, “Crystals with disordered hydrogen-bond networks and superprotonic conductivity. Review,” *Crystallogr. Rep.* **48**, 1012–1037 (2003).
- ⁹Y. Matsuda, M. Yonemura, H. Koga, C. Pitteloud, M. Nagao, M. Hirayama, and R. Kanno, “Synthesis, crystal structure, and ionic conductivity of tunnel structure phosphates, RbMg_{1-x}H_{2x}(PO₃)₃·y(H₂O),” *J. Mater. Chem. A* **1**, 15544–15551 (2013).
- ¹⁰A. I. Baranov, L. A. Shuvalov, and N. M. Shchagina, “Superion conductivity and phase transitions in CsHSO₄ and CsHSeO₄ crystals,” *JETP Lett.* **36**, 459–462 (1982).
- ¹¹A. Ishikawa, H. Maekawa, T. Yamamura, Y. Kawakita, K. Shibata, and M. Kawai, “Proton dynamics of CsH₂PO₄ studied by quasi-elastic neutron scattering and PFG-NMR,” *Solid State Ionics* **179**, 2345–2349 (2008).
- ¹²R. Blinc, V. Dimic, J. Petkovšek, and E. Pirkmajer, “Study of proton dynamics in paraelectric KH₂PO₄ by quasi-elastic cold neutron scattering,” *Phys. Lett. A* **26**, 8–9 (1967).
- ¹³S. Ikeda, Y. Noda, H. Sugimoto, and Y. Yamada, “Dynamical properties of protons in KH₂PO₄ studied by incoherent neutron scattering,” *J. Phys. Soc. Jpn.* **63**, 1001–1008 (1994).
- ¹⁴A. Hartl, S.-H. Park, M. Hoelzel, N. Paul, and R. Gilles, “Proton conductivity in a hureaulite-type compound, Mn₅[(PO₄)₂(PO₃(OH))₂](HOH)₄,” *J. Solid State Chem.* **277**, 290–302 (2019).
- ¹⁵S.-H. Park, A. Hartl, D. Sheptyakov, M. Hoelzel, and A. Arauzo, “Structural investigation into magnetic spin orders of a manganese phosphatic oxyhydroxide, Mn₅[(PO₄)₂(PO₃(OH))₂](HOH)₄,” *Symmetry* **13**, 1688 (2021).
- ¹⁶M. Baum, F. Rieutord, F. Juranyi, C. Rey, and D. Rébiscoul, “Dynamical and structural properties of water in silica nanoconfinement: Impact of pore size, ion nature, and electrolyte concentration,” *Langmuir* **35**, 10780–10794 (2019).
- ¹⁷X. Liu, Y. Li, J. Xue, W. Zhu, J. Zhang, Y. Yin, Y. Qin, K. Jiao, Q. Du, B. Cheng, X. Zhuang, J. Li, and M. D. Guiver, “Magnetic field alignment of stable proton-conducting channels in an electrolyte membrane,” *Nat. Commun.* **10**, 842 (2019).
- ¹⁸G. Xing, T. Yan, S. Das, T. Ben, and S. Qiu, “Synthesis of crystalline porous organic salts with high proton conductivity,” *Angew. Chem., Int. Ed.* **57**, 5345–5349 (2018).
- ¹⁹H. Matsui and M. Tadokoro, “Eigen-like hydrated protons traveling with a local distortion through the water nanotube in new molecular porous crystals {[M^{III}(H₂bim)₃](TMA)-20H₂O}_n (M = Co, Rh, Ru),” *J. Chem. Phys.* **137**, 144503 (2012).
- ²⁰N. Zhang, Y. Song, J. Huo, Y. Li, Z. Liu, J. Bao, S. Chen, X. Ruan, and G. He, “Formation mechanism of the spiral-like structure of a hydrogen bond network confined in a fluorinated nanochannel: A molecular dynamics simulation,” *J. Phys. Chem. C* **121**, 13840–13847 (2017).
- ²¹M. Sadakiyo, T. Yamada, and H. Kitagawa, “Rational designs for highly proton-conductive metal-organic frameworks,” *J. Am. Chem. Soc.* **131**, 9906–9907 (2009).
- ²²M. A. Belyanchikov, M. Savinov, Z. V. Bedran, P. Bednyakov, P. Proschek, J. Prokleska, V. A. Abalmasov, J. Petzelt, E. S. Zhukova, V. G. Thomas, A. Dudka, A. Zhugayevych, A. S. Prokhorov, V. B. Anzin, R. K. Kremer, J. K. H. Fischer, P. Lunkenheimer, A. Loidl, E. Uykur, M. Dressel, and B. Gorshunov, “Dielectric ordering of water molecules arranged in a dipolar lattice,” *Nat. Commun.* **11**, 3927 (2020).
- ²³M. Busch, T. Hofmann, B. Frick, J. P. Embs, B. Dyatkin, and P. Huber, “Ionic liquid dynamics in nanoporous carbon: A pore-size- and temperature-dependent neutron spectroscopy study on supercapacitor materials,” *Phys. Rev. Mater.* **4**, 055401 (2020).
- ²⁴A. B. Yaroslavlsev, “Proton conductivity of inorganic hydrates,” *Russ. Chem. Rev.* **63**, 429–435 (1994).
- ²⁵Rigaku Oxford Diffraction UK Ltd, CrysAlisPro, 2015.
- ²⁶V. Petricek, M. Dusek, and L. Palatinus, “Crystallographic computing system JANA2006: General features,” *Z. Kristallogr. - Cryst. Mater.* **229**, 345–352 (2014).
- ²⁷R. T. Azuah, L. R. Kneller, Y. Qiu, P. L. W. Tregenna-Piggott, C. M. Brown, J. R. D. Copley, and R. M. Dimeo, “DAVE: A comprehensive software suite for the reduction, visualization, and analysis of low energy neutron spectroscopic data,” *J. Res. Natl. Inst. Stand. Technol.* **114**, 341–358 (2009).
- ²⁸R. Böhmer, M. Maglione, P. Lunkenheimer, and A. Loidl, “Radio-frequency dielectric measurements at temperatures from 10 to 450 K,” *J. Appl. Phys.* **65**, 901–904 (1989).
- ²⁹D. Marx and J. Hutter, *Ab Initio Molecular Dynamics: Basic Theory and Advanced Methods* (Cambridge University Press, Cambridge, 2009).
- ³⁰T. D. Kühne, M. Iannuzzi, M. Del Ben, V. V. Rybkin, P. Seewald, F. Stein, T. Laino, R. Z. Khaliullin, O. Schütt, F. Schiffmann, D. Golze, J. Wilhelm, S. Chulkov, M. H. Bani-Hashemian, V. Weber, U. Borštnik, M. TAILLEFUMIER, A. S. Jakobovits, A. Lazzaro, H. Pabst, T. Müller, R. Schade, M. Guidon, S. Andermatt, N. Holmberg, G. K. Schenter, A. Hehn, A. Bussy, F. Belleflamme, G. Tabacchi, A. Glöb, M. Lass, I. Bethune, C. J. Mundy, C. Plessl, M. Watkins, J. VandeVondele, M. Krack, and J. Hutter, “CP2K: An electronic structure and molecular dynamics software package—Quickstep: Efficient and accurate electronic structure calculations,” *J. Chem. Phys.* **152**, 194103 (2020).
- ³¹J. Vandevondele, M. Krack, F. Mohamed, M. Parrinello, T. Chassaing, and J. Hutter, “QUICKSTEP: Fast and accurate density functional calculations using a mixed Gaussian and plane waves approach,” *Comput. Phys. Commun.* **167**, 103–128 (2005).
- ³²S. Goedecker, M. Teter, and J. Hutter, “Separable dual-space Gaussian pseudopotentials,” *Phys. Rev. B* **54**, 1703–1710 (1996).
- ³³C. Hartwigsen, S. Goedecker, and J. Hutter, *Phys. Rev. B* **58**, 3641–3662 (1998).
- ³⁴M. Krack, “Pseudopotentials for H to Kr optimized for gradient-corrected exchange-correlation functionals,” *Theor. Chem. Acc.* **114**, 145–152 (2005).
- ³⁵J. VandeVondele and J. Hutter, “Gaussian basis sets for accurate calculations on molecular systems in gas and condensed phases,” *J. Chem. Phys.* **127**, 114105 (2007).
- ³⁶J. P. Perdew, K. Burke, and M. Ernzerhof, “Generalized gradient approximation made simple,” *Phys. Rev. Lett.* **77**, 3865 (1996).
- ³⁷S. Grimme, J. Antony, S. Ehrlich, and H. Krieg, “A consistent and accurate *ab initio* parametrization of density functional dispersion correction (DFT-D) for the 94 elements H–Pu,” *J. Chem. Phys.* **132**, 154104 (2010).
- ³⁸G. Kresse and J. Furthmüller, “Efficient iterative schemes for *ab initio* total-energy calculations using a plane-wave basis set,” *Phys. Rev. B* **54**, 11169–11186 (1996).
- ³⁹G. Kresse and D. Joubert, “From ultrasoft pseudopotentials to the projector augmented-wave method,” *Phys. Rev. B* **59**, 1758–1775 (1999).
- ⁴⁰M. Brehm and B. Kirchner, “TRAVIS—A free analyzer and visualizer for Monte Carlo and molecular dynamics trajectories,” *J. Chem. Inf. Model.* **51**, 2007–2023 (2011).
- ⁴¹M. Brehm, M. Thomas, S. Gehrke, and B. Kirchner, “TRAVIS—A free analyzer for trajectories from molecular simulation,” *J. Chem. Phys.* **152**, 164105 (2020).
- ⁴²W. Humphrey, A. Dalke, and K. Schulten, “VMD: Visual molecular dynamics,” *J. Mol. Graphics* **14**, 33–38 (1996).

- ⁴³H. Euchner, M. Mihalkovič, F. Gähler, M. R. Johnson, H. Schober, S. Rols, E. Suard, A. Bosak, S. Ohhashi, A. P. Tsai, S. Lidin, C. P. Gomez, J. Custers, S. Paschen, and M. De Boissieu, "Anomalous vibrational dynamics in the $\text{Mg}_2\text{Zn}_{11}$ phase," *Phys. Rev. B* **83**, 144202 (2011).
- ⁴⁴M. Thomas, M. Brehm, R. Fligg, P. Vöhringer, and B. Kirchner, "Computing vibrational spectra from *ab initio* molecular dynamics," *Phys. Chem. Chem. Phys.* **15**, 6608–6622 (2013).
- ⁴⁵T. Famprikis, P. Canepa, J. A. Dawson, M. S. Islam, and C. Masquelier, "Fundamentals of inorganic solid-state electrolytes for batteries," *Nat. Mater.* **18**, 1278–1291 (2019).
- ⁴⁶B. Frick, J. Combet, and L. Van Eijck, "New possibilities with inelastic fixed window scans and linear motor Doppler drives on high resolution neutron backscattering spectrometers," *Nucl. Instrum. Methods Phys. Res., Sect. A* **669**, 7–13 (2012).
- ⁴⁷M. T. F. Telling, L. Clifton, J. Combet, B. Frick, S. Howells, and V. G. Sakai, "Lyophilised protein dynamics: More than just methyls?," *Soft Matter* **8**, 9529–9532 (2012).
- ⁴⁸J. P. Embs, F. Juranyi, and R. Hempelmann, "Introduction to quasielastic neutron scattering," *Z. Phys. Chem.* **224**, 5–32 (2010).
- ⁴⁹*Broadband Dielectric Spectroscopy*, edited by F. Kremer and A. Schönhal (Springer, Berlin, 2002).
- ⁵⁰P. Lunkenheimer and A. Loidl, "Dielectric spectroscopy on organic charge-transfer salts," *J. Phys.: Condens. Matter* **27**, 373001 (2015).
- ⁵¹P. Lunkenheimer, S. Krohns, S. Riegg, S. G. Ebbinghaus, A. Reller, and A. Loidl, "Colossal dielectric constants in transition-metal oxides," *Eur. Phys. J.: Spec. Top.* **180**, 61–89 (2010).
- ⁵²S. Emmert, M. Wolf, R. Gulich, S. Krohns, S. Kastner, P. Lunkenheimer, and A. Loidl, "Electrode polarization effects in broadband dielectric spectroscopy," *Eur. Phys. J. B* **83**, 157–165 (2011).
- ⁵³M. D. Ediger, C. A. Angell, and S. R. Nagel, "Supercooled liquids and glasses," *J. Phys. Chem.* **100**, 13200–13212 (1996).
- ⁵⁴P. Lunkenheimer and A. Loidl, "Glassy dynamics: From millihertz to terahertz," in *The Scaling of Relaxation Processes*, edited by F. Kremer and A. Loidl (Springer International Publishing, Cham, 2018), pp. 23–59.
- ⁵⁵C. A. Angell, "Strong and fragile liquids," in *Relaxations in Complex Systems*, edited by K. L. Ngai and G. B. Wright (Springer, New York, 1985), pp. 3–11.
- ⁵⁶R. Böhmer, K. L. Ngai, C. A. Angell, and D. J. Plazek, "Nonexponential relaxations in strong and fragile glass formers," *J. Chem. Phys.* **99**, 4201–4209 (1993).
- ⁵⁷W. M. Du, G. Li, H. Z. Cummins, M. Fuchs, J. Toulouse, and L. A. Knauss, "Light-scattering study of the liquid-glass transition in propylene carbonate," *Phys. Rev. E* **49**, 2192–2205 (1994).
- ⁵⁸A. Faraone, D. V. Wagle, G. A. Baker, E. C. Novak, M. Ohl, D. Reuter, P. Lunkenheimer, A. Loidl, and E. Mamontov, "Glycerol hydrogen-bonding network dominates structure and collective dynamics in a deep eutectic solvent," *J. Phys. Chem. B* **122**, 1261–1267 (2018).
- ⁵⁹S. Kämmerer, W. Kob, and R. Schilling, "Test of mode coupling theory for a supercooled liquid of diatomic molecules. II. *q*-dependent orientational correlators," *Phys. Rev. E* **58**, 2141–2150 (1998).
- ⁶⁰W. Götze and T. Voigtman, "Universal and nonuniversal features of glassy relaxation in propylene carbonate," *Phys. Rev. E* **61**, 4133–4147 (2000).
- ⁶¹M. Winkler, P. Lunkenheimer, A. Loidl, S.-H. Park, B. Röska, and M. Hoelzel, "Charge transport by global protonic conductivity and relaxational dynamics over hydrogen bonds in $\text{Fe}^{2+}\text{Fe}^{3+}_{3.2}(\text{Mn}^{2+}, \text{Zn})_{0.8}(\text{PO}_4)_3(\text{OH})_{4.2}(\text{HOH})_{0.8}$," *Solid State Ionics* **347**, 115240 (2020).
- ⁶²S. L. Hutton, I. Fehst, R. Böhmer, M. Braune, B. Mertz, P. Lunkenheimer, and A. Loidl, "Proton glass behavior and hopping conductivity in solid solutions of anti-ferroelectric betaine phosphate and ferroelectric betaine phosphite," *Phys. Rev. Lett.* **66**, 1990–1993 (1991).
- ⁶³Y. Feng, C. Ancona-Torres, T. F. Rosenbaum, G. F. Reiter, D. L. Price, and E. Courtens, "Quantum and classical relaxation in the proton glass," *Phys. Rev. Lett.* **97**, 145501 (2006).
- ⁶⁴N. H. Bashian, S. Zhou, M. Zuba, A. M. Ganose, J. W. Stiles, A. Ee, D. S. Ashby, D. O. Scanlon, L. F. J. Piper, B. Dunn, and B. C. Melot, "Correlated polyhedral rotations in the absence of polarons during electrochemical insertion of lithium in ReO_3 ," *ACS Energy Lett.* **3**, 2513–2519 (2018).
- ⁶⁵A. Hartl, "Proton motions in hydrogen bonds of phosphatic oxyhydroxides: The case of $\text{Mn}^{2+}[(\text{PO}_4)_2(\text{PO}_3\text{OH})_2](\text{HOH})_4$," MS thesis, Ludwig Maximilian University, Munich, 2020.